



Calhoun: The NPS Institutional Archive
DSpace Repository

Theses and Dissertations

1. Thesis and Dissertation Collection, all items

1968-09

The Effect of Stagnation Temperature and Molecular Weight Variation on Gaseous Injection Into A Supersonic Stream.

Chrans, Larry "J"

Monterey, California. Naval Postgraduate School

<http://hdl.handle.net/10945/40047>

This publication is a work of the U.S. Government as defined in Title 17, United States Code, Section 101. Copyright protection is not available for this work in the United States.

Downloaded from NPS Archive: Calhoun



Calhoun is the Naval Postgraduate School's public access digital repository for research materials and institutional publications created by the NPS community. Calhoun is named for Professor of Mathematics Guy K. Calhoun, NPS's first appointed -- and published -- scholarly author.

Dudley Knox Library / Naval Postgraduate School
411 Dyer Road / 1 University Circle
Monterey, California USA 93943

<http://www.nps.edu/library>

UNITED STATES NAVAL POSTGRADUATE SCHOOL



THESIS

THE EFFECT OF STAGNATION TEMPERATURE AND
MOLECULAR WEIGHT VARIATION ON GASEOUS
INJECTION INTO A SUPERSONIC STREAM

by

Larry "J" Chrans

September 1968

THESIS
C4489



THE EFFECT OF STAGNATION TEMPERATURE AND MOLECULAR WEIGHT
VARIATION ON GASEOUS INJECTION INTO A SUPERSONIC STREAM

by

Larry "J" Chrans
Lieutenant, United States Navy
B.S.M.E., University of Nebraska, 1958

Submitted in partial fulfillment of the
requirements for the degree of

AERONAUTICAL ENGINEER

From the

NAVAL POSTGRADUATE SCHOOL
September 1968

Signature of Author

Larry J. Chrans

Approved by

Daniel J. Collins

Thesis Advisor

Allen E. Fuhs

Chairman, Department of Aeronautics

W. F. Koehler for R. F. Rinehart

Academic Dean

ABSTRACT

The purpose of this study was to investigate the effect of injectant stagnation temperature and molecular weight variation on the flow field generated from secondary injection of a gas normal to a supersonic stream. Experiments were conducted at a primary stream Mach number of 2.80 in the Naval Postgraduate School supersonic wind tunnel. Experimental data have been correlated with various theories, showing both agreement and disagreement. Data presented include penetration of secondary jet into primary flow and shock shape as correlated with the second order blast wave theory.

TABLE OF CONTENTS

CHAPTER	PAGE
I. INTRODUCTION	11
II. EXPERIMENTAL EQUIPMENT	13
III. THEORETICAL ANALYSIS	16
Penetration Height	17
Blast Wave Analogy	21
IV. EXPERIMENTAL RESULTS	26
Penetration Height	27
Shock Radius	32
V. CONCLUSIONS	35
REFERENCES	39
APPENDIX	41

LIST OF TABLES

TABLE	PAGE
I. Sonic Nozzle Calibration	44

LIST OF FIGURES

FIGURE		PAGE
1.	Injection Equipment Arrangement	45
2.	Photograph of Equipment Layout	46
3.	Photograph of Test Section Area	46
4.	Photograph of Heater Assembly	47
5.	Stagnation Pressure-Temperature Assembly . . .	48
6.	Sonic Nozzle Diagram	49
7.	Static Pressure Tap Locations	50
8.	Schetz and Billig Flow Pattern for an Underexpanded Jet	51
9.	Zukoski and Spaid Flow Model	51
10.	Hsia Flow Model	52
11.	Broadwell Flow Model	52
12.	Experimental Run Matrix	53
13.	Schlieren Photograph--Run Number 21	54
14.	Schlieren Photograph--Run Number 70	55
15.	Penetration Height--Argon	56
16.	Penetration Height--Nitrogen	57
17.	Penetration Height--Helium	58
18.	Composite Plot of Figures 15, 16 and 17	59
19.	Penetration Height--Mass Flow Rate Constant . .	60
20.	Shock Radius--Argon	61
21.	Shock Radius--Nitrogen	62
22.	Shock Radius--Helium	63
23.	Shock Radius--Varying Molecular Weight	64

FIGURE		PAGE
24.	Non-dimensional Plot of Figure 20	65
25.	Non-dimensional Plot of Figure 21	66
26.	Non-dimensional Plot of Figure 22	67
27.	Composite Plot of Figures 24, 25 and 26	68
28.	Shock Radius--Mass Flow Constant, Varying Temperature	69
29.	Shock Radius--Mass Flow Constant, Varying Molecular Weight	70
30.	Non-dimensional Plot of Figure 28	71
31.	Non-dimensional Plot of Figure 29	72
32.	Comparison of Characteristic Dimensions-- Varying Temperature	73
33.	Comparison of Characteristic Dimensions-- Mass Flow Constant	74
34.	Comparison of Characteristic Dimensions-- Varying Molecular Weight	75
35.	Shock Radius--Comparison with Penetration Height at Varying Temperature	76

LIST OF SYMBOLS

<u>Symbol</u>	<u>Definition</u>
A	area
C_D	drag coefficient
C_p	pressure coefficient
c	nozzle discharge coefficient
c_p	specific heat at constant pressure
d	diameter
E	energy, measured per unit length, released in the creation of a shock wave
h	penetration height of secondary fluid into primary stream
Δh	energy transferred from secondary to primary stream
J_o	function of γ_∞ in the blast wave analogy
K	flow coefficient through a flowmeter
M	Mach number
\dot{m}	mass flow rate
P	pressure
$\Delta P'$	pressure differential across an orifice
R	radius of bow wave measured perpendicular to the flat plate axis
\bar{R}	non-dimensional blast wave radius
R_j	gas constant of fluid j
R_o	characteristic radius related to the blast wave energy
r	nose radius of equivalent blunt body
T	temperature

<u>Symbol</u>	<u>Definition</u>
t	time
V	velocity
W	molecular weight
x	distance along flat plate axis
\bar{x}	x/R_o
Y	expansion factor of flow through an orifice meter
θ	angle between surface of flat plate and injector nozzle axis
β	ratio of orifice diameter to pipe diameter
γ	specific heat ratio
ρ	density
λ_1	function of γ_o in the blast wave analogy

Superscript

* pertaining to sonic conditions

Subscripts

j injectant or secondary fluid
 ∞ primary fluid
 o stagnation conditions
 1 upstream from flowmeter orifice
 2 orifice conditions

CHAPTER I

INTRODUCTION

The interaction of a lateral jet with a supersonic stream is of fundamental importance to the understanding of complex supersonic flows. The jet interaction application to thrust vector control, reaction control jets and fuel injection for supersonic combustion is of great engineering interest. Although extensive investigations¹⁻⁵ have been conducted of the supersonic gaseous injection phenomena, no systematic investigation of secondary jet stagnation temperature and molecular weight has been made. Most investigations have used sonic injection, so that in the absence of stagnation temperature and molecular weight variations it has not been possible to distinguish between the effects of jet momentum and jet mass addition.

The objective of this thesis was to study the flow field induced by injecting a gas normal to a supersonic stream, where the primary interest was to discover the effect of injectant stagnation temperature and molecular weight in the flow field. These studies were performed in the Naval Postgraduate School supersonic wind tunnel at a Mach number of 2.80 by injecting gaseous nitrogen, argon and helium through a sonic nozzle mounted normal to a flat plate. The parameters varied during the experiments include injectant stagnation pressure and temperature, mass flow rate, molecular weight and injector exit area. By

variation of injectant stagnation temperature and molecular weight, distinctions are made between jet mass and jet momentum effects.

CHAPTER II

EXPERIMENTAL EQUIPMENT

The injection equipment used in this thesis was arranged as in Figure 1. Compressed bottles of gaseous injectant were obtained commercially and fed into the system through a pressure regulator. The flow was then passed through a flow-meter, into the heater, and on to the sonic nozzle mounted in the flat plate. Photographs of the equipment assembly are shown in Figures 2 and 3.

The method used to heat the secondary gas was simple, yet effective. Twenty-five feet of 3/8 inch O.D. stainless steel tube were coiled and placed in an insulated container as shown in Figure 4. Preliminary calculations indicated sonic velocity would be reached inside the heater tube at high temperature and pressure for standard tube diameters smaller than that used. An arc welder was then connected across the ends of the coil, and the coil was heated by passing an electric current through the stainless steel tube. The injectant gas was subsequently heated through contact with the hot tube. The maximum injectant temperature was set at 1800°R due to the structural integrity of the heater at high pressures.

At the heater exit and just prior to the sonic nozzle entrance a device was installed (Figure 5) to decrease the velocity of the secondary flow to approximately stagnation conditions. The flow velocity was gently decreased through

a 5 degree diverging section until the cross-sectional area was increased by a factor of ten, ensuring the velocity of the flow through the enlarged section to be less than 0.06 Mach (or approximately stagnation conditions). At this point the temperature and pressure of the secondary fluid were measured, and these values were used in the isentropic equations for a sonic nozzle. A well rounded converging nozzle was then used to decrease the area ratio prior to entering the sonic nozzle.

The sonic nozzle was a simple converging nozzle with parallel side walls at the exit section as shown in Figure 6. Exit diameters of 0.1406 inches and 0.075 inches were used during the experiments. The sonic nozzle was calibrated by means of an ASME sharp-edged orifice meter. The nozzle discharge coefficient was found to be 0.96 as summarized in the Appendix.

A special phenolic supersonic tunnel block was fabricated to allow the flat plate pedestal to be mounted on the test section floor. The sonic nozzle could then be inserted through the bottom of the test section and through the pedestal without disturbing the flat plate. Thirty-nine static pressure taps were located on the surface of the plate as shown in Figure 7. The generated pressures were measured with a mercury manometer. The side force data will not be discussed in this thesis.

The NPGS supersonic wind tunnel is a blow-down model with a 4 inch by 4 inch test section, 6 inches long. The

tunnel is capable of 5 minutes of continuous operation at a stagnation pressure of 50 psia. The Reynolds number at the injector port was 8.5×10^6 inches/inch for $M = 2.8$, ensuring a turbulent boundary layer in the region of the injector nozzle.

The Schlieren system used had a standard off-set arrangement with collimating mirrors used in place of lenses. The mirrors, light source, and camera were positioned with the aid of a surveyor's transit, so that most of the parallax in the system was eliminated. With this arrangement, shadow-graphs could also be obtained by removing the knife-edge and changing the slit-source to a point-source.

CHAPTER III

THEORETICAL ANALYSIS

Two properties of the interaction phenomena, penetration height of the secondary fluid and radius of the induced bow shock, will be treated extensively in this thesis.

The secondary gas is injected into a supersonic stream in the form of a highly underexpanded jet, as illustrated by Schetz and Billig¹ in Figure 8. The secondary jet penetrates the primary stream to a certain height before it is completely bent over and proceeds downstream with the primary fluid. This penetration height depends on the properties of the two streams. Figures 9 and 10 illustrate interaction models by Zukoski and Spaid³ and Hsia,⁶ respectively. In each of these a penetration height is defined, and the induced shock is noted.

The radius of the induced bow shock can be treated as a function of the penetration height of the secondary fluid³ or may be calculated from the second order blast wave analogy, as presented by Broadwell⁷ and Dahm.⁸ Figure 11 shows Broadwell's flow model where only the radius of the induced shock is being considered.

It is interesting to note that each of the flow models shown in Figures 9 through 11 was based on a blunt-body approximation of the interaction phenomena, but that the results obtained by the model originators varied considerably, due to the basic assumptions made.

The above models were used in this thesis as a guide for determining which parameters of the flow to vary and then were compared with the experimental results.

PENETRATION HEIGHT

Zukoski and Spaid,³ in investigating the injection phenomena, obtained their scaling laws for secondary injection by setting up a model for a solid body, which would give a shock pattern similar to that produced by injection. By balancing the drag of the nose section of the blunt body against the momentum flux of the injectant, the characteristic dimension of the nose section could be found. They assumed the blunt body to be a quarter sphere and using Newtonian flow calculations found the force in the direction of the primary flow to be

$$F_x = (\pi/8) M_\infty^2 \gamma_\infty C_p h^2 P_\infty \quad (1)$$

where h is the radius of the quarter sphere and

$$C_p = C_p(M_\infty, \gamma_\infty)$$

is evaluated at the nose of the body.

By injecting the secondary gas normal to a flat plate, the only contribution to the momentum in the direction along the plate will be that obtained from the expansion of the secondary fluid to the primary stream pressure. From the steady flow energy equation,

$$h_{0j} = h_j + V_j^2/2$$

or

$$V_j^2 = 2 c_{p_j} T_{O_j} (1 - T_j/T_{O_j}) \quad (2)$$

Assuming expansion to the primary stream pressure P_∞ , the expression for the velocity V_j can be written as

$$V_j = \left\{ \frac{2\gamma_j}{\gamma_j - 1} R_j T_{O_j} \left[1 - \frac{1}{1 + \frac{\gamma_\infty - 1}{2} M_\infty^2} \left(\frac{P_{O_\infty}}{P_{O_j}} \right)^{\frac{\gamma_j - 1}{\gamma_j}} \right] \right\}^{\frac{1}{2}} \quad (3)$$

or in terms of temperature,

$$V_j = \left\{ \frac{2\gamma_j}{\gamma_j - 1} R_j T_{O_j} \left[1 - \frac{1}{1 + \frac{\gamma_\infty - 1}{2} M_\infty^2} \left(\frac{T_{O_\infty}}{T_{O_j}} \right) \right] \right\}^{\frac{1}{2}} \quad (4)$$

The mass flow rate through a sonic nozzle with an effective exit area of CA_j^* , where C is the discharge coefficient of the nozzle, is given by

$$\dot{m}_j = CA_j^* P_{O_j} \left[\frac{1}{R_j T_{O_j}} \right]^{\frac{1}{2}} \left[\gamma_j \left(\frac{2}{\gamma_j + 1} \right)^{\frac{\gamma_j + 1}{\gamma_j - 1}} \right]^{\frac{1}{2}} \quad (5)$$

The force balance in the primary stream direction due to the momentum flux is then

$$F_x = \dot{m}_j V_j \quad (6)$$

Equating (1) and (6), Zukoski and Spaid³ solved for the radius h of the quarter sphere and found

$$\frac{h}{d\sqrt{c}} = \frac{1}{M_\infty} \left(\frac{P_{O_j}}{P_\infty} \frac{\gamma_j}{\gamma_\infty} \frac{2}{c_p} \right)^{\frac{1}{2}} \left[\frac{2}{\gamma_j - 1} \left(\frac{2}{\gamma_j + 1} \right)^{\frac{\gamma_j + 1}{\gamma_j - 1}} \left(1 - \frac{T_\infty}{T_{O_j}} \right) \right]^{\frac{1}{4}} \quad (7)$$

or in terms of stagnation conditions

$$\frac{h}{d\sqrt{c}} = \frac{1}{M_\infty} \left(1 + \frac{\gamma_\infty - 1}{2} M_\infty^2 \right)^{\frac{\gamma_\infty}{2(\gamma_\infty - 1)}} \left(\frac{P_{Oj}}{P_{O_\infty}} \frac{\gamma_j}{\gamma_\infty} \frac{2}{C_p} \right)^{\frac{1}{2}} \left[\frac{2}{\gamma_j - 1} \left(\frac{2}{\gamma_j + 1} \right)^{\frac{\gamma_j + 1}{\gamma_j - 1}} \left(1 + \frac{1}{1 + \frac{\gamma_\infty - 1}{2} M_\infty^2} \frac{T_{O_\infty}}{T_{Oj}} \right) \right]^{\frac{1}{4}} \quad (8)$$

They then proposed that this calculated radius could be used as a measure of the scale of the disturbance produced by injection. Further, if the model is correct, it is expected that other flow features will also be proportional to changes in h .

Hsia⁶ also assumed that the nature and extent of flow disturbances resulting from secondary injection are the same as those created by a blunt-nosed slender body. He then equated the nose drag of the slender body to the drag derived from momentum exchange between the primary and secondary streams and the effective force resulting from energy exchange due to reaction and evaporation, giving

$$C_D A (\rho_\infty V_\infty^2 / 2) = \dot{m}_j V_\infty (1 \pm \frac{\Delta h}{V_\infty^2})$$

where A is the projected area of the body in the direction of flow, ρ_∞ and V_∞ are the density and velocity of the undisturbed flow region, \dot{m}_j is the flow rate of the secondary fluid, and Δh is the energy exchanged per unit mass of the injectant due to chemical reaction and evaporation between the primary and secondary fluids. Assuming that the shape

of the equivalent body was a quarter sphere followed by a half cylinder, Hsia found the nose radius to be given by

$$r = \left(\frac{4}{\pi C_D} \right)^{\frac{1}{2}} \left(1 + \frac{h}{V_{\infty}^2} \right)^{\frac{1}{2}} \left(\frac{\dot{m}_j}{\rho_{\infty} V_{\infty}} \right)^{\frac{1}{2}} \quad (9)$$

This can be thought of as the effective penetration height the secondary fluid would reach for a given flow rate of the secondary fluid.

Although both theories discussed above use a blunt-body model, the use of two different velocities leads to a fundamental difference. Zukoski and Spaid³ assumed the secondary fluid expanded to the primary stream pressure, P_{∞} , after leaving the injector nozzle, and therefore the final velocity attained was the velocity due to isentropic expansion to that pressure. Hsia⁶ assumed the final velocity attained by the secondary fluid was that of the primary stream, V_{∞} . This led to a penetration height by Hsia that was jet mass dependent and a penetration height by Zukoski and Spaid that was jet momentum dependent.

The secondary mass flow from a sonic nozzle is proportional to the stagnation pressure, P_{0j} , and inversely proportional to the stagnation temperature, T_{0j} , of the secondary fluid. The momentum of the secondary fluid leaving the injector nozzle is only proportional to the stagnation pressure of the secondary fluid. The depth of penetration of the secondary fluid into the primary stream will be either jet mass or jet momentum dependent, or a combination of both. Agreement between the Zukoski-Spaid³ and Hsia⁶

penetration theory has been previously noted,⁶ but in the absence of stagnation temperature variation no distinction can be made between the jet mass or the jet momentum effects.

BLAST WAVE ANALOGY

The radius of the bow shock caused by secondary injection has been derived in terms of the second order blast wave equation. Dahm⁸ and Broadwell⁷ based their theories on the blast wave analogy, where it was assumed that:

- (a) Injection of a secondary fluid causes the same pressure, velocity and density fields as a blunt-nosed body in a hypersonic stream.
- (b) The secondary fluid is accelerated to the primary stream velocity, V_{∞} .
- (c) The energy added per unit length of gas is equal to the change in momentum of the secondary fluid and the heat added to the primary fluid.
- (d) The blast wave analogy is valid throughout the entire region of the interaction of the primary and secondary streams.

It can be noted again that Zukoski and Spaid³ also assumed a blunt-nosed body in a hypersonic stream (Newtonian calculations) to find the penetration height of the injectant, but assumed the final velocity the secondary fluid reached was that from expanding to the primary stream pressure, P_{∞} , instead of the primary stream velocity, V_{∞} .

The models of Broadwell⁷ and Dahm⁸ were based on the blast wave analogy of Hayes.⁹ According to Hayes' concept

of hypersonic similitude, the pressure, density and velocity fields generated by an unyawed, axisymmetric body in a uniform hypersonic flow field are similar to the pressure, density and velocity fields generated by the explosion of a line charge. Once the pressure, density and velocity fields as a function of time t and distance from the line R have been obtained, the corresponding fields for the axisymmetric body are derived by replacing t by x/V_∞ , where V_∞ is the velocity of the undisturbed primary flow and x is the distance along the axis of the flat plate from the apex of the detached shock. The concept of similitude is completed by relating the energy released by the line charge to the drag of the body.

Sakurai's¹⁰ second order solution for the shock wave radius R at any time t in the unsteady problem is given by

$$R = \left(\frac{2E}{\pi J_0 P_\infty} \right)^{\frac{1}{4}} \left[1 - \lambda_1 \left(\frac{J_0 P_\infty}{2E} \right)^{\frac{1}{2}} c_\infty t \right]^{\frac{1}{2}} \left(c_\infty t \right)^{\frac{1}{2}} \quad (10)$$

where J_0 and λ_1 are constants that depend on the specific heat ratio γ_∞ (for $\gamma_\infty = 1.4$, $J_0 = 0.88$ and $\lambda_1 = -1.989$), P_∞ and c_∞ are the pressure and sound speed of the undisturbed primary fluid, and E is the energy, measured per unit length, released in the creation of the shock wave. Assuming $t = x/V_\infty$, and $ct = x/M_\infty$, equation (10) reduces to

$$\bar{R} = \left(\frac{4}{J_0} \right)^{\frac{1}{4}} \left(\frac{\bar{x}}{M_\infty} \right)^{\frac{1}{2}} \left[1 - \lambda_1 \frac{J_0}{2} \frac{\bar{x}}{M_\infty} \right]^{\frac{1}{2}} \quad (11)$$

where x is the distance measured from the apex of the bow shock along the centerline of the flat plate, V_∞ is the

velocity of the primary fluid at the injectant station,
 $\bar{R} = R/R_0$, $\bar{x} = x/R_0$ and

$$R_0 = (E/2\pi P_\infty)^{\frac{1}{2}} \quad (12)$$

is the characteristic radius related to the blast wave energy.

As Broadwell⁷ pointed out, E is the energy per unit length in the completely symmetrical case, and for a flat plate all the energy is confined above the plate. Therefore, E/2 should be set equal to the total increase in energy due to injection.

As stated in (c) the total energy added per unit length is equal to the change in momentum of the secondary fluid and the heat added to the primary fluid. Broadwell⁷ derived the energy term as

$$E = 2 \dot{m}_j V_\infty \left[1 + \frac{2 + (\gamma_\infty - 1) M_\infty^2}{2 (\gamma_\infty - 1) M_\infty^2} \frac{W_\infty}{W_j} \frac{T_{0j}}{T_{0\infty}} \right] \quad (13)$$

where the first term represents the energy related to the drag caused by the injectant fluids, and the second term represents the effect of the volume addition by the injectant gas. The development of the energy term by Dahm⁸ parallels and extends that of Broadwell⁷ but employs significantly different approaches in certain important areas. Dahm derived the energy term for the second order blast wave radius as

$$E = 2 \dot{m}_j V_\infty \left[\frac{1}{2} + \frac{1}{\gamma_\infty (\gamma_\infty - 1) M_\infty^2} + \frac{\gamma_j}{\gamma_j - 1} \frac{2 + (\gamma_\infty - 1) M_\infty^2}{2 \gamma_\infty M_\infty^2} \frac{W_\infty}{W_j} \frac{T_{Oj}}{T_{O_\infty}} \right. \\ \left. + \left(\frac{\gamma_j}{\gamma_\infty} \frac{W_\infty}{W_j} \frac{T_{Oj}}{T_{O_\infty}} \right)^{\frac{1}{2}} \frac{M_j}{M_\infty} \left(\frac{2 + (\gamma_\infty - 1) M_\infty^2}{2 + (\gamma_j - 1) M_j^2} \right) \cos \theta \right] \quad (14)$$

where θ is the angle between the surface of the plate and the axis of the injector ($\cos \theta = 0$ for normal injection). The terms in the energy equation denote the increase in kinetic energy of the secondary fluid, a mass correction term, the heat added to the primary stream, and the effect of injecting at an angle.

It is interesting to note that although Broadwell developed the energy term, E , from an entirely different viewpoint than that of Dahm, his result agrees very closely for normal injection.

Taking Dahm's value for E , for normal injection equation (12) reduces to

$$R_O = \left[\frac{\dot{m}_j V_\infty}{\pi P_\infty} \left(\frac{1}{2} + \frac{1}{\gamma_\infty (\gamma_\infty - 1) M_\infty^2} + \frac{\gamma_j}{\gamma_j - 1} \frac{2 + (\gamma_\infty - 1) M_\infty^2}{2 \gamma_\infty M_\infty^2} \frac{W_\infty}{W_j} \frac{T_{Oj}}{T_{O_\infty}} \right) \right]^{\frac{1}{2}} \quad (15)$$

Expanding equation (15) in terms of the stagnation properties of the primary and secondary streams and assuming a constant primary stream molecular weight, specific heat ratio and Mach number, then

$$R_O \propto \left[\dot{m}_j \frac{T_{O_\infty}^{\frac{1}{2}}}{P_{O_\infty}} \left(A + \frac{\gamma_j}{(\gamma_j - 1) W_j} \frac{T_{Oj}}{T_{O_\infty}} \right) \right]^{\frac{1}{2}} \quad (16)$$

where A is a constant that depends on M_∞ . Since

$$\dot{m}_\infty \propto A_\infty^* \frac{P_{O_\infty}}{T_{O_\infty}^{\frac{\gamma}{2}}}$$

where A_∞^* is the throat area of the primary nozzle,

$$R_O \propto \left[\frac{\dot{m}_j}{\dot{m}_\infty} \left(A + \frac{\gamma_j}{(\gamma_j - 1)W_j} \frac{T_{Oj}}{T_{O_\infty}} \right) \right]^{\frac{1}{2}} \quad (17)$$

Further reduction may be made if for a particular secondary fluid both the primary and secondary flow rates are held constant. Then,

$$R_O \propto \left[A + B \frac{T_{Oj}}{T_{O_\infty}} \right]^{\frac{1}{2}} \quad (18)$$

where $B = B(\gamma_j, W_j)$ and $A = A(M_\infty)$.

CHAPTER IV

EXPERIMENTAL RESULTS

All parameters associated with the primary stream were held constant throughout these experiments. That is, air was used as the primary fluid, and the supersonic tunnel stagnation temperature and pressure, and tunnel Mach number were essentially constant for all runs. Therefore, when it is stated that the pressure ratio or mass ratio was varied, in effect, only the injectant pressure or mass was varied. The injectant stagnation pressure was varied from 12.5 psi to 300 psi, giving a range of pressure ratios from $\frac{1}{4}$ to 6. The injectant stagnation temperature was varied from room temperature (520° R) to 1590° R, giving a range of temperature ratios from 1 to 3. Nitrogen, argon, and helium were used as injectant gases to provide a substantial range for molecular weight effects and also to provide for any heat capacity ratio effects. The sonic nozzle exit diameter was also varied to change the mass flow rate of the injectant while keeping the pressure and temperature constant.

The individual experimental runs were conducted in the order shown in Figure 12. Schlieren photographs were taken of each run, and shadowgraph photographs were taken of many runs. In general the shadowgraph pictures taken did not add to the detail found in the Schlieren pictures and, therefore, were not extensively used. The static pressures displayed on the manometer board were also photographed at the same time

the Schlieren photographs were taken. Polaroid type 55 P/N film was used for each Schlieren picture so that the negatives could be enlarged for comparison. The data taken from the photographs, which included penetration height of the injectant and radius of the bow wave, were obtained by either magnifying the photograph and measuring directly or placing the negative in an optical comparator. Seventy-seven individual runs were made for this thesis, each one varying the parameters of the injectant. Typical Schlieren photographs obtained are shown in Figures 13 and 14.

The experimental results are presented in two sections. Figures 15 through 20 depict the penetration heights obtained by varying each parameter of the secondary flow, and Figures 21 through 31 illustrate the variation of the bow shock radius under the same conditions.

PENETRATION HEIGHT

The depth of penetration of the secondary fluid into the primary stream was scaled directly from the photographs and was taken to be the maximum height reached by the bent-over highly underexpanded jet. Figures 15, 16, and 17 show the penetration heights attained by argon, nitrogen, and helium respectively. In each figure the penetration height is plotted as a function of the stagnation pressure ratio, with the runs at various temperatures and nozzle exit diameters included. In each of these figures reference is made to the Zukoski and Spaid³ theory for penetration height, showing agreement with their predictions. Although the stagnation

temperature ratio was varied by a factor of three while holding the pressure ratio constant, no essential differences in the penetration height could be detected. Increasing the stagnation temperature of the secondary fluid while holding the pressure constant causes the secondary mass flow rate to decrease. Since the penetration height of the secondary fluid was not affected by this action, either the penetration height is a function of the secondary momentum or is at most a weak function of T_{o_j}/T_{o_∞} . It should be noted that the slope of the line indicating the Zukoski-Spauid theory does not coincide exactly with that plotted from the experimental values obtained. This difference may be attributed to the exact value of the exponent of the pressure ratio term in equation (8).

It may be noted in Figure 17 that considerably fewer data points are indicated. In general, it was found that for the same quality Schlieren photograph the underexpanded helium jet was much more difficult to detect than was the argon or nitrogen jet.

Figure 18 is a composite plot of Figures 15, 16 and 17, showing the mean penetration heights of the three gases as a function of the stagnation pressure ratio. As indicated there is a difference in the penetration heights of the three gases. Zukoski and Spauid's equation (8) is not a function of molecular weight; however, it does provide for heat capacity ratio variations. Argon and helium, having the same value of heat capacity ratio, should have identical

penetration heights under the conditions presented. Nitrogen, having a smaller value of heat capacity ratio, should have a penetration height 4 per cent higher than that of argon and helium, as calculated from equation (8). This is indeed the case when comparing the penetration heights of nitrogen and helium, but argon lies 10 per cent above nitrogen and 14 per cent above helium. This result shows that the penetration height is a function of the molecular weight.

Equation (8) may be put in the form

$$h \propto \left(\frac{2\gamma_j}{\gamma_j - 1} \right)^{\frac{1}{4}} \left(R_j T_{Oj} \right)^{\frac{1}{4}} \frac{1}{M_\infty} \left(\frac{\dot{m}_j}{P_\infty} \right)^{\frac{1}{2}}, \quad \frac{P_\infty}{P_{Oj}} \ll 1 \quad (19)$$

Holding the primary stream parameters and the secondary mass flow rate constant, equation (19) can be further reduced to

$$h \propto \left(\frac{2\gamma_j}{\gamma_j - 1} \right)^{\frac{1}{4}} \left(R_j T_{Oj} \right)^{\frac{1}{4}} \quad (20)$$

Experiments were next conducted to investigate the penetration height while holding the secondary mass flow rate constant. For each gas considered the stagnation pressure and temperature were adjusted to give a mass flow rate of 0.0065 lbs/sec and 0.010 lbs/sec. The results are presented in Figure 19. It is evident that for a given mass flow rate, the penetration height increases with an increasing stagnation temperature ratio and also increases with a decreasing molecular weight. At a constant stagnation temperature of 795°R, the following results were obtained from Figure 19, using equation (20):

Calculated

$$\frac{h_{N_2}}{h_A} = 1.19$$

$$\frac{h_{He}}{h_A} = 1.78$$

$$\frac{h_{He}}{h_{N_2}} = 1.50$$

Measured

$$\frac{h_{N_2}}{h_A} = 1.11$$

$$\frac{h_{He}}{h_A} = 1.89$$

$$\frac{h_{He}}{h_{N_2}} = 1.70$$

Disregarding the heat capacity ratio dependence of the penetration height, i.e., the term

$$[2\gamma_j/(\gamma_j - 1)]^{\frac{1}{4}}$$

produces:

Calculated

$$\frac{h_{N_2}}{h_A} = 1.093$$

$$\frac{h_{He}}{h_A} = 1.78$$

$$\frac{h_{He}}{h_{N_2}} = 1.63$$

Measured

$$\frac{h_{N_2}}{h_A} = 1.11$$

$$\frac{h_{He}}{h_A} = 1.89$$

$$\frac{h_{He}}{h_{N_2}} = 1.70$$

Disregarding the heat capacity ratio dependence of the penetration height can be viewed as changing the characteristic velocity of the secondary momentum. If the velocity at the sonic nozzle exit, v^* , is used in equation (8) in place of V_j , then the results obtained from Figure 19, using equation (20), are:

Calculated

$$\frac{h_{N_2}}{h_A} = 1.05$$

$$\frac{h_{He}}{h_A} = 1.78$$

$$\frac{h_{He}}{h_{N_2}} = 1.69$$

Measured

$$\frac{h_{N_2}}{h_A} = 1.11$$

$$\frac{h_{He}}{h_A} = 1.89$$

$$\frac{h_{He}}{h_{N_2}} = 1.70$$

The calculated values using V^* are in better agreement with the experimental results than those using V_j .

The data shown in Figure 19 scale as the $\frac{1}{2}$ power of \dot{m}_j . When the heat capacity ratio dependence was neglected, the data also scaled approximately as the $\frac{1}{4}$ power of the molecular weight, which is in agreement with the theory. The relatively large difference between the measured h_{He}/h_A ratio and the expected value is attributed to a molecular weight effect.

For a given gas (constant molecular weight) and the above stated conditions,

$$h \propto (T_{O_j})^{\frac{1}{4}}$$

There is an expected increase in penetration height of 32 per cent between the temperature of 530°R and 1590°R for all gases. Measured values found from Figure 19 were 44 per cent increase for argon, 33 per cent for nitrogen, and 12 per cent for helium. The lighter molecular weight gases show less variation with T_{O_j} than predicted by theory.

SHOCK RADIUS

Figures 20 through 22 show the shock radius variation for the various gases at a constant pressure ratio, varying temperature. The radius R was measured perpendicular to the flat plate axis at distances x downstream from the injector axis. This presented a fixed reference point from which the actual shock radius could be measured. Comparing these figures, it is apparent that as the molecular weight of the injectant gas decreases, a greater variation occurs in the shock radius with temperature.

Figure 23 shows the variation of the bow shock with molecular weight, while holding the stagnation pressure ratio and temperature ratio constant. Examination of equations (11) and (17) indicates that the radius of the bow shock should vary approximately as $\dot{m}_j^{\frac{1}{4}} (A + BR_j)^{\frac{1}{2}}$ for these conditions, where $A = A(M_\infty)$ and $B = B(\gamma_j, T_{O_j})$.

The variation of the bow wave with temperature and molecular weight was very evident when viewing the radius of the bow wave. When this radius is non-dimensionalized with respect to the characteristic radius, R_0 , related to the blast wave energy, the effect is a convergence of all radii into a single line. This has been shown quite well in Figures 24, 25, and 26 respectively. The second order blast wave prediction, equation (11), has been added to these graphs to show the relationship between theory and measured values. In each case the measured values followed the pattern set by the second order theory with what appears

to be a constant displacement. However, when the mean lines from the three gases are placed on a composite plot, as in Figure 27, a molecular weight dependence is present. The spread between the three gases, as compared with any measurement error, is too large to be taken as experimental scatter. It may be noted that if a proper scaling radius, R_0 , based on E , is selected, then all curves should collapse to a single line.

Equation (18) was used as the basis for the next set of experiments, where the injectant mass flow rate was held constant and the radius R was viewed as a function of T_{oj} , W_j and γ_j . Figure 28 shows the variation of the shock radius with injectant stagnation temperature. Equation (18) was used to predict the increase of the radius with temperature with the following results:

Calculated	Measured
$\frac{R_{1590}}{R_{530}} = 1.10$	$\frac{R_{1590}}{R_{530}} = 1.13$
$\frac{R_{1060}}{R_{530}} = 1.06$	$\frac{R_{1060}}{R_{530}} = 1.06$

Equation (18) was then used to predict the increase of the radius with molecular weight and heat capacity ratio effects, as shown in Figure 29. The results were:

Calculated	Measured
$\frac{R_{He}}{R_A} = 1.23$	$\frac{R_{He}}{R_A} = 1.29$

$$\frac{R_{N_2}}{R_A} = 1.04$$

$$\frac{R_{He}}{R_{N_2}} = 1.17$$

$$\frac{R_{N_2}}{R_A} = 1.06$$

$$\frac{R_{He}}{R_{N_2}} = 1.22$$

In general, equation (18) showed excellent agreement for the constant secondary mass flow case. Figures 30 and 31 are the non-dimensional plot of Figures 28 and 29 respectively. Again the three separate radii collapse into a single line when put in the non-dimensional form of equation (11). Some differences due to molecular weight effects may be noticeable in Figure 31.

CHAPTER V

CONCLUSIONS

At constant P_{Oj} , varying T_{Oj} , the penetration height theory of Zukoski and Spaid³ showed good agreement with experimental results. The penetration height also showed some dependence on molecular weight, which is contrary to theory.

When the secondary mass flow rate was held constant, the penetration height varied with T_{Oj} . This rules out any theory based strictly upon a jet mass dependence, as proposed by Hsia⁶ in equation (9).

The penetration height scaled as $(\dot{m}_j)^{\frac{1}{2}}$ as predicted by all theories.

Ignoring heat capacity ratio effects, the penetration height scaled roughly as $(R_j)^{\frac{1}{4}}$ which is in agreement with the jet momentum theory of Zukoski and Spaid. Assuming a different characteristic velocity of the secondary flow (using V^* instead of V_j), good agreement was obtained with theory without having to ignore the heat capacity ratio effects ($V^* = [\gamma_j R_j T_j]^{\frac{1}{2}}$ for a sonic nozzle). If the heat capacity ratio effects were also ignored using this new characteristic velocity V^* , then the results reduced to that obtained using V_j . V^* is therefore a better characteristic velocity for the flow process than V_j .

In general, the penetration height, as a function of T_{Oj} , differed for different molecular weights. This is not in agreement with theory. When considered as a function of

P_{O_j} , the experimental results for the penetration height showed good agreement with the theory of Zukoski and Spaid for both the constant P_{O_j} and constant mass flow runs. The conclusion is that the penetration height is not a function of T_{O_j} or is, at most, a weak function of T_{O_j} .

The radius of the blast wave measured from the experimental data was in close agreement with that predicted by Dahm. The blast wave theory was not able to predict the molecular weight variation accurately when the pressure and temperature of the system were varied (Figure 23) but showed good agreement when the secondary mass flow was held constant.

The penetration height, h , was found to remain constant for varying temperature, and the bow shock radius, R , did not. Therefore, h would not be a good choice as a characteristic dimension to represent the entire interaction phenomena. An attempt was made to non-dimensionalize the height of penetration with respect to the characteristic blast wave radius, R_0 , with the results shown in Figures 32 through 34. Figure 32 shows the variation of h/R_0 with respect to pressure for flows at various temperatures. The temperature spread is due to the fact that h does not vary with temperature, while R_0 does. Figure 33 indicates that as T_{O_j}/T_{O_∞} increases at constant mass flow, there is a divergence of the three gases, with respect to h/R_0 . This is because h does not vary as T_{O_j} increases while R_0 does vary as a function of temperature with another function of molecular weight included. Typical values are:

$$\begin{array}{ll}
 \text{argon} & R_o \propto \left[0.728 + 0.427 T_{o_j}/T_{o_\infty} \right]^{\frac{1}{2}} \\
 \text{nitrogen} & R_o \propto \left[0.728 + 0.848 T_{o_j}/T_{o_\infty} \right]^{\frac{1}{2}} \\
 \text{helium} & R_o \propto \left[0.728 + 4.28 T_{o_j}/T_{o_\infty} \right]^{\frac{1}{2}}
 \end{array}$$

Figure 34 indicates the molecular weight effect present in the above terms at constant temperature.

One statement that can be made of all three figures is that the slopes of their lines are near zero. This would indicate that a correction term in Dahm's energy equation might be enough to cause all the slopes to reach zero.

Figure 35 shows the effect of non-dimensionalizing the bow shock radius with respect to the penetration height as formulated in equation (8). This can be compared with the results obtained in Figure 26, which shows the bow shock non-dimensionalized with respect to the characteristic blast wave radius. The blast wave radius, R_o , appears to be a better characteristic dimension for the shock radius.

In general, the comparisons between the characteristic dimensions, h and R_o , and the experimental data indicate that h would be a good engineering correlation parameter for secondary nitrogen and argon flows but would be less accurate for the lighter molecular weight gases such as helium.

Further, the data would support the contention that the heating of a lighter molecular weight gas would be more effective in increasing the area of interaction than the

heating of a heavier molecular weight gas. Since the aerodynamic interaction force would be proportional to the interaction area, the heating of a lighter molecular weight gas would generate more side force than a heavier molecular weight gas. This advantage of increase in side force is particularly evident in the case of constant mass flow of a lighter molecular weight gas.

Differences between the experimental results and the theoretical predictions due to molecular weight effects may be caused by the mixing processes of the secondary gas with the primary stream.

In general, the concept of jet mass or jet momentum dependence proved to be a useful tool in arranging the experiments to study the parameters involved.

REFERENCES

1. Schetz, J. A. and Billig, F. S., "Penetration of Jets into a Supersonic Stream," J. Spacecraft and Rockets, 3, 1658-1665 (1966).
2. Hawk, N. E. and Amick, J. L., "Two-Dimensional Secondary Interaction with a Supersonic Stream," AIAA J., 5, 655-660 (1967).
3. Zukoski, E. E. and Spaid, F. W., "Secondary Injection of Gases into a Supersonic Flow," AAIA J., 2, 1689-1696 (1964).
4. Walker, R. E., Stone, A. R. and Shandor, M., "Secondary Gas Injection in a Conical Rocket Nozzle," AAIA J., 1, 334-338 (1963).
5. Horton, T. R. and Meade, A. J., "Thrust Vector Control of Rocket Engines by Gaseous Injection: A Critical Appraisal of Theoretical Models," R.P.E. Tech. Report No. 67/7 (1967).
6. Hsia, H. T. S., "Equivalence of Secondary Injection to a Blunt Body in Supersonic Flow," AIAA J., 4, 1832-1834 (1966).
7. Broadwell, J. E., "Analysis of the Fluid Mechanics of Secondary Injection for Thrust Vector Control," AIAA J., 1, 1067-1075 (1963).
8. Dahm, T. J., "The Development of an Analogy to Blast-Wave Theory for the Prediction of Interaction Forces Associated with Gaseous Secondary Injection into a Supersonic Stream," VIDYA TN 9166-TN-3, May 1964.

9. Hayes, W. D., "On Hypersonic Similitude," Quart. J. Appl. Math., 5, 105 (1947).
10. Sakurai, A., "On the Propagation and Structure of a Blast Wave," J. Phys. Soc. Japan, 8, 652-659, Part I (1953); 9, 256-266, Part II (1954).
11. Stearns, R. F., et al., Flow Measurement with Orifice Meters, Van Nostrand Co., Inc., New York, 1951.
12. Shapiro, A. H., The Dynamics and Thermodynamics of Compressible Fluid Flow, Vols. 1 and 2, The Ronald Press Company, New York, (1953).

APPENDIX I

The sonic nozzle becomes a flow metering device whenever the ratio of the exit pressure to the isentropic stagnation pressure is less than the critical pressure. When this occurs, the mass flow rate through the sonic nozzle is given by

$$\dot{m}_j = A_j^* \frac{P_{Oj}}{\sqrt{T_{Oj}}} \left[\frac{\gamma_j}{R_j} \left(\frac{2}{\gamma_j + 1} \right)^{\frac{\gamma_j + 1}{\gamma_j - 1}} \right]^{\frac{1}{2}} \quad (30)$$

A stagnation temperature-pressure reservoir was installed just prior to the sonic nozzle which allowed measurement of the stagnation temperature and pressure used in the above equation.

The sonic nozzle was calibrated by means of an ASME sharp-edged orifice flowmeter, which was built to ASME standards as set forth in Reference 11. The flowmeter was a standard 2-inch diameter pipe with an orifice designed to give an orifice-to-pipe diameter ratio β of 0.15. This value of β ensured that the Reynolds number through the orifice would always be greater than 10,000 for the range of mass flow rates considered. Vena contracta pressure taps were located across the orifice plate, and the static pressure and temperature within the flowmeter were measured at a point 6 diameters upstream from the orifice.

The pressure differential across the orifice was in the range of 0.5 to 1.5 psi for the mass flow rates considered during calibration. An attempt was made to measure this

differential with a pressure transducer, but none were available that would give the precision required at these low differentials. A mercury U-tube manometer was then fabricated by milling $\frac{1}{4}$ inch semicircular slots in 1 inch thick plexiglass and bonding the two halves together. The result was a 2-inch thick plexiglass U-tube manometer capable of withstanding 300 psi pressure, with no apparent effects from creep. This performed satisfactorily during calibration, and pressure differentials could be read to a precision of 0.05 psi. The plexiglass U-tube manometer was calibrated against a standard glass-tube manometer, with no differences detected.

The mass flow rate through a sharp-edged orifice flow-meter is given by

$$\dot{m} = YKA_2 \left[2 \rho_1 \Delta P' \right]^{\frac{1}{2}}$$

where Y (Expansion Factor) is determined by

$$Y = 1 - \left[.41 + .35 (A_2/A_1)^2 \right] F'/\gamma_1 P_1 \quad (31)$$

for vena contracta taps,

K = flow coefficient

= 0.6133 to 0.5995 for $Re = 10,000$ to $100,000$

and $\beta = 0.15$

A_2 = orifice area

A_1 = pipe area

ρ_1 = density upstream of the orifice

$\Delta P'$ = pressure differential across the orifice

P_1 = pressure upstream of the orifice

Table I shows the values obtained during calibration of the 0.1406 inch diameter sonic nozzle.

The sonic nozzle discharge coefficient, c , was defined as the ratio of the actual nozzle flow (flow measured through the sharp-edged orifice) to the flow calculated from the isentropic laws for a sonic nozzle,

$$c = \frac{\dot{m}_{ACT}}{ISENTROPIC \text{ FLOW RATE}}$$

For well-designed nozzles with straight axes having "pipe" Reynolds numbers measured at the minimum area of 10^6 or more, the discharge coefficient is of the order of 0.99.¹² The pipe Reynolds numbers during calibration ranged from 5.4×10^4 to 1.4×10^5 , and therefore slightly less discharge coefficients were obtained.

All nozzles used were checked to determine that their discharge coefficients fell in the same range as the one calibrated.

TABLE I

SONIC NOZZLE CALIBRATION

Run #	P ₁ psia	P _{0j} psia	T _{0j} R	T ₁ R	P' in. Hg	Y	K	\dot{m} S.N. lbs/sec	\dot{m} ASME lbs/sec	c
1	50.0	40.8	527°	527°	1.96	0.9941	0.6013	0.01486	0.01403	0.956
2	49.9	40.6	527	527	1.95	.9942	.6013	.01461	.01398	.957
3	50.0	40.7	530	530	1.95	.9942	.6013	.01460	.01395	.956
4	50.1	41.1	605	530	1.75	.9948	.6014	.01380	.01324	.960
5	50.0	41.2	651	528	1.61	.9952	.6017	.01333	.01273	.955
6	50.2	41.6	720	528	1.48	.9956	.6018	.01281	.01223	.955
7	50.3	41.7	788	528	1.39	.9959	.6020	.01227	.01187	.958
8	50.0	41.6	879	528	1.26	.9962	.6022	.01159	.01123	.973
9	50.1	41.8	1019	528	1.09	.9958	.6026	.01082	.01051	.972
10	50.0	41.8	1167	528	.98	.9970	.6029	.01011	.00996	.985
11	100.0	34.5	610	529	2.80	.9958	.5991	.02452	.02362	.963
12	100.9	36.4	1246	529	1.95	.9971	.6000	.02022	.01986	.982
13	99.7	34.7	1564°	529°	1.47	0.9978	0.6004	0.01769	0.01716	0.970

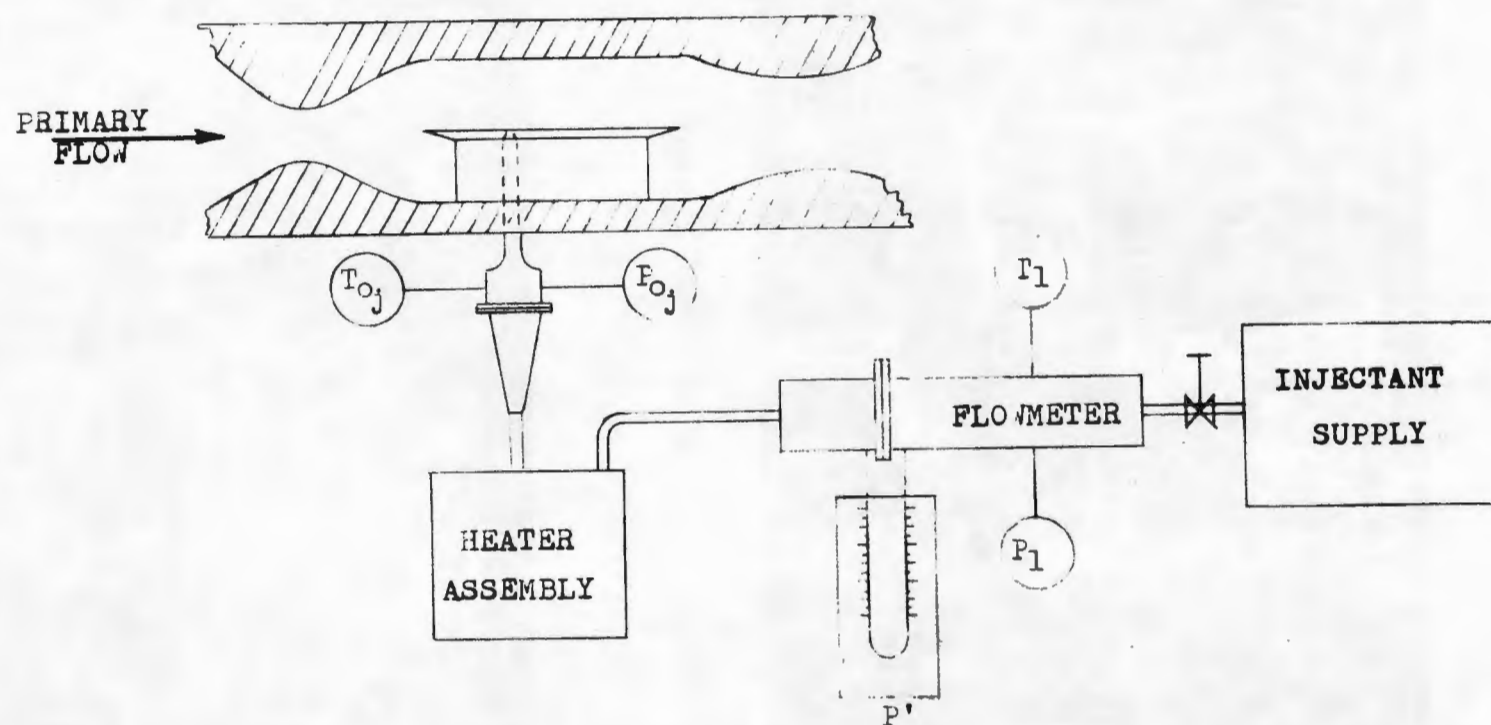


Figure 1. Injection Equipment Arrangement.



Figure 2. Photograph of Equipment Layout.

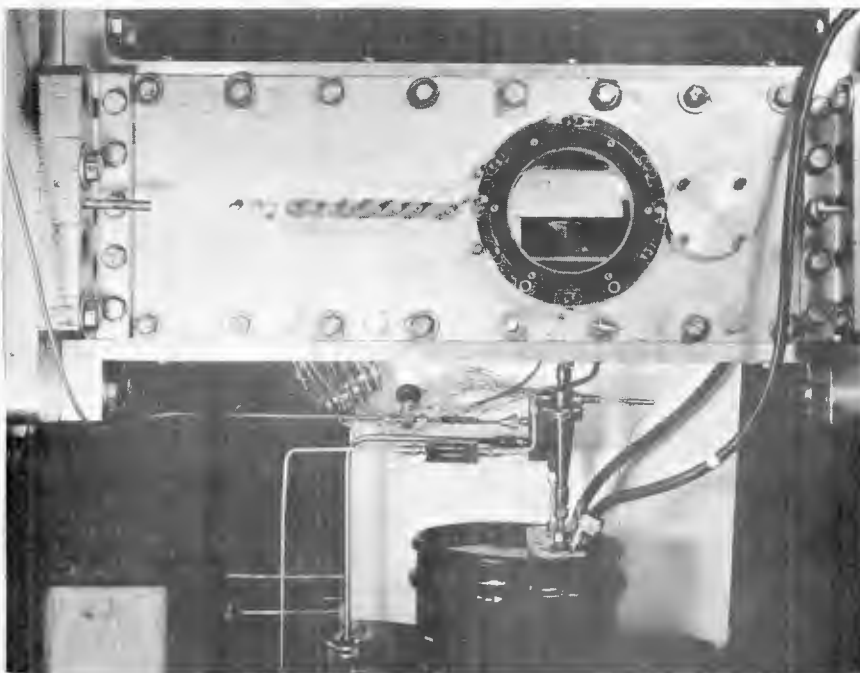
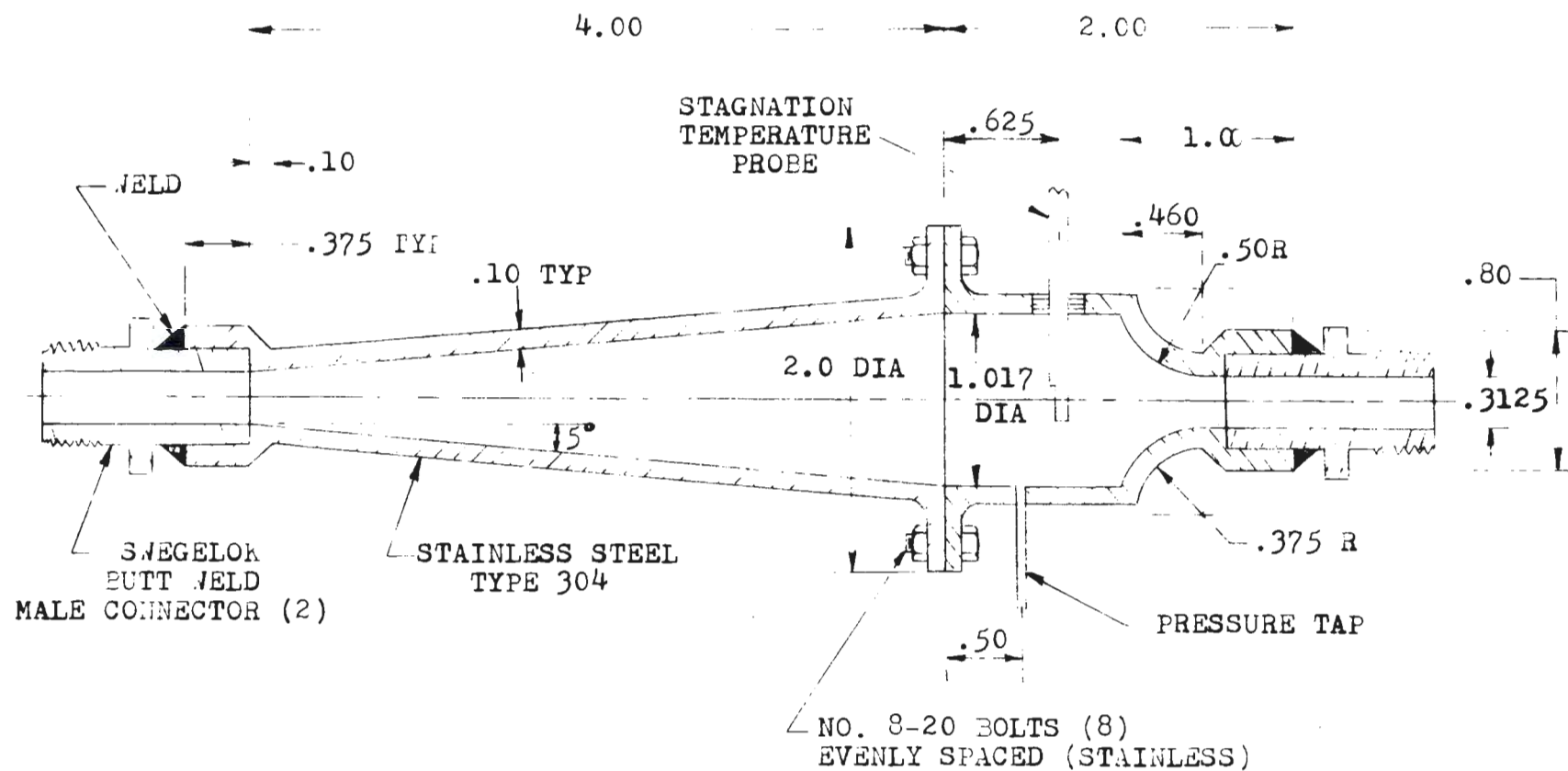


Figure 3. Photograph of Test Section Area.

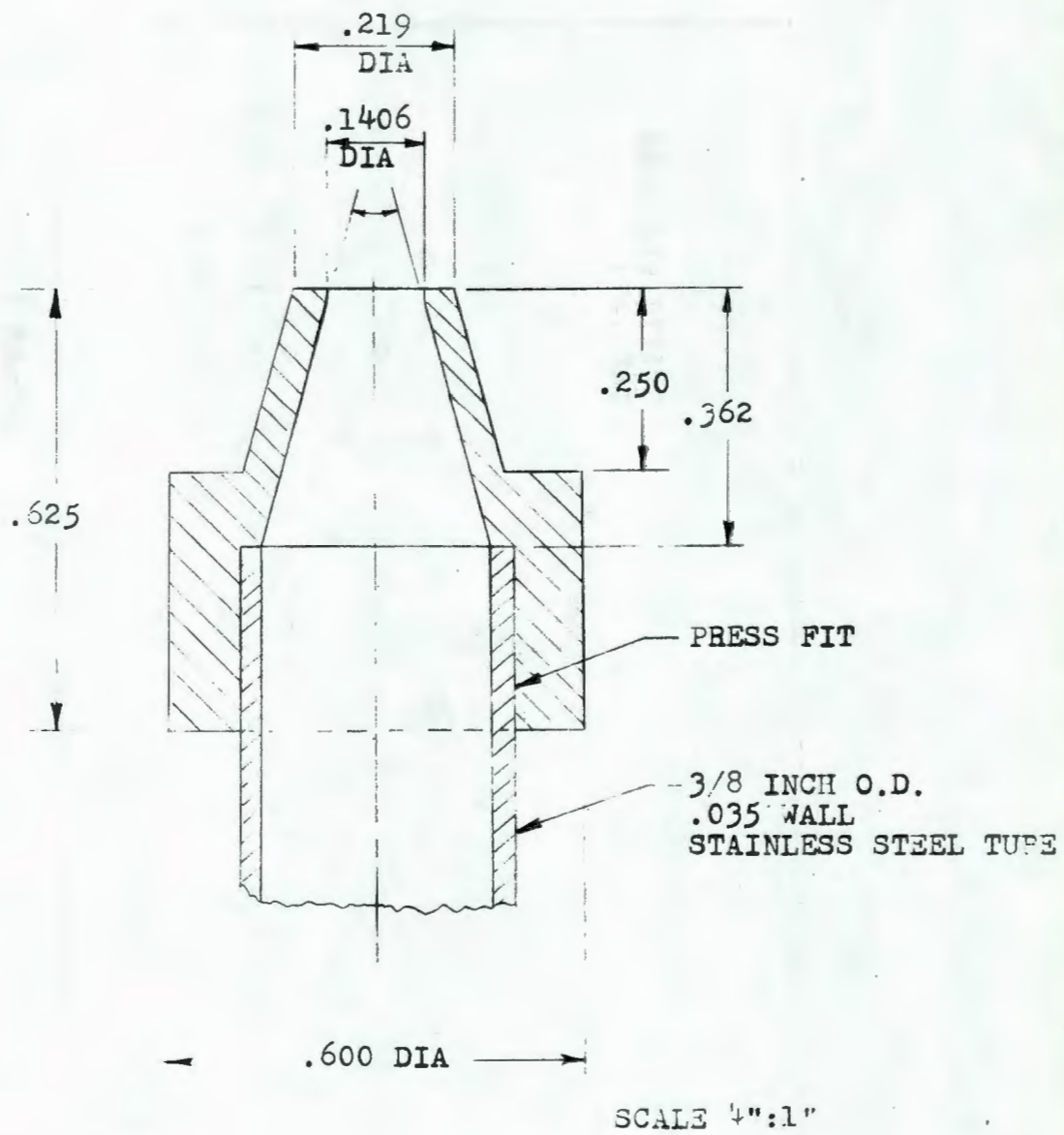


Figure 4. Photograph of Heater Assembly.



All dimensions are in inches

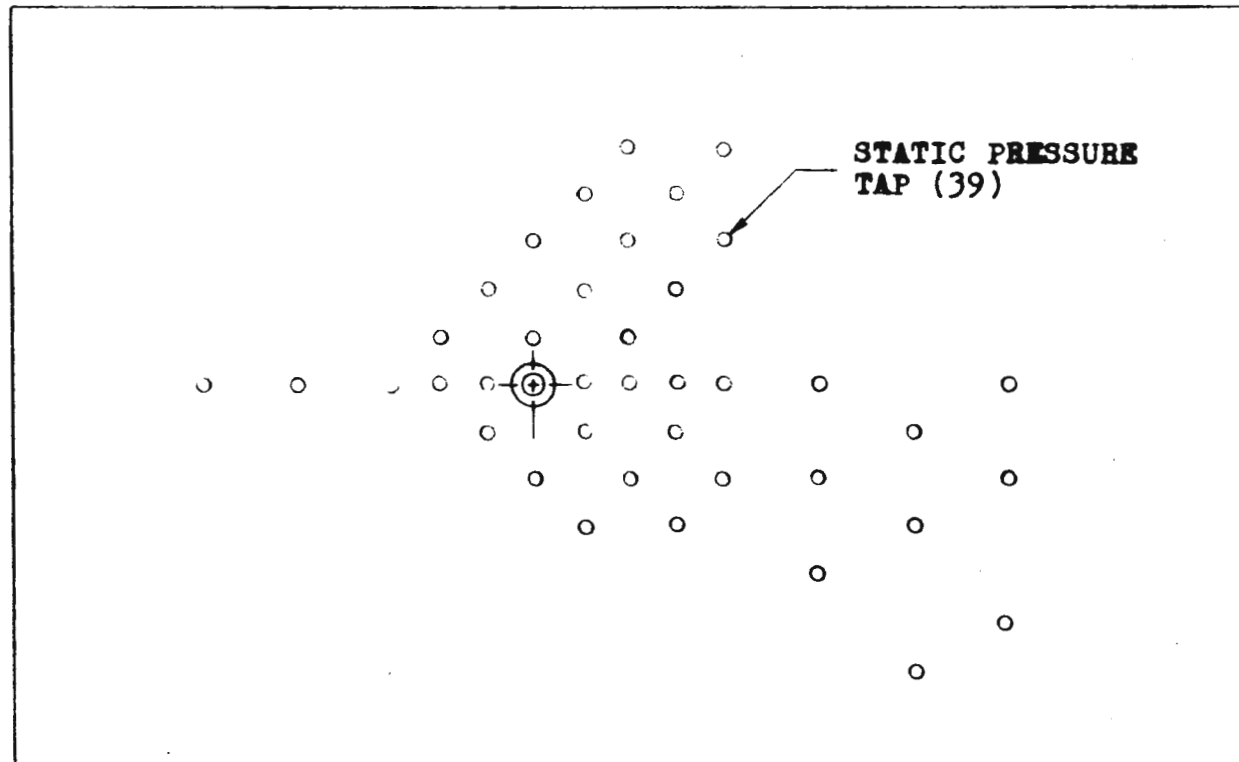
Figure 5. Stagnation Pressure-Temperature Assembly.



All dimensions are in inches.

Figure 6. Sonic Nozzle Diagram.

PRIMARY
FLOW



SCALE 1":1"

Figure 7. Static Pressure Tap Locations.

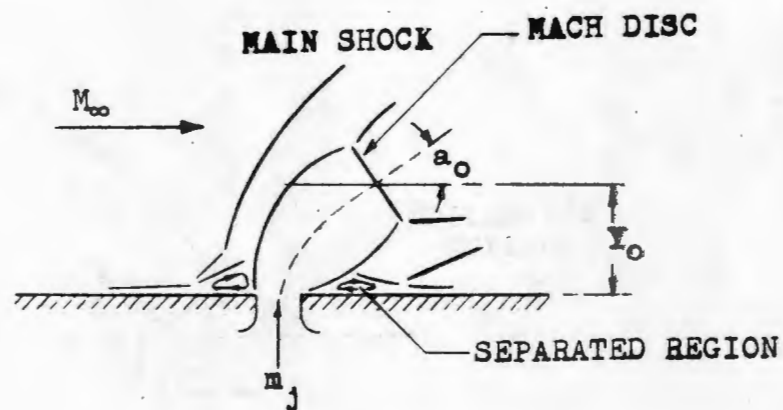


Figure 8. Schetz and Billig Flow Pattern for an Underexpanded Jet.

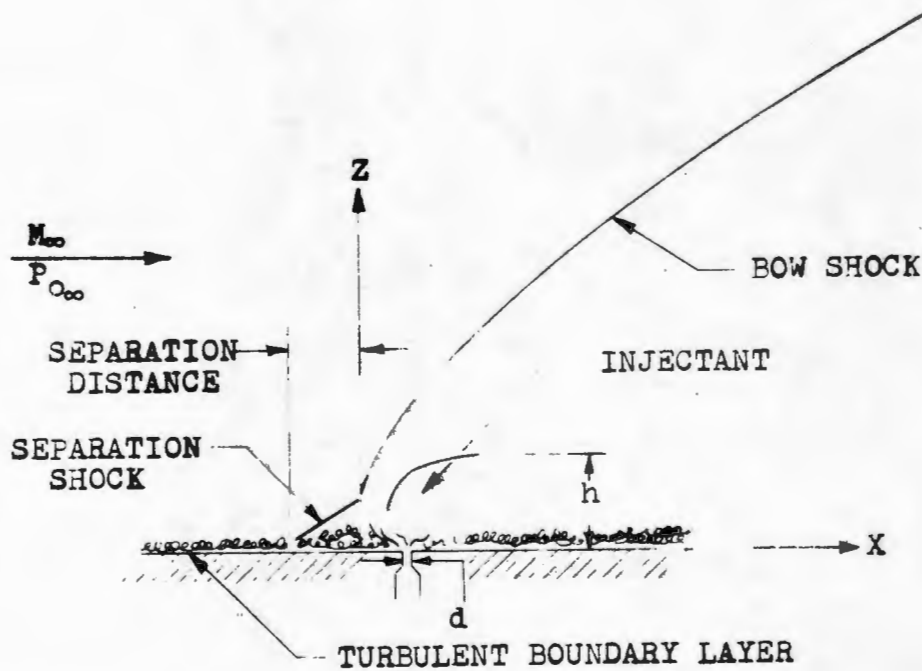


Figure 9. Zukoski and Spaid Flow Model.

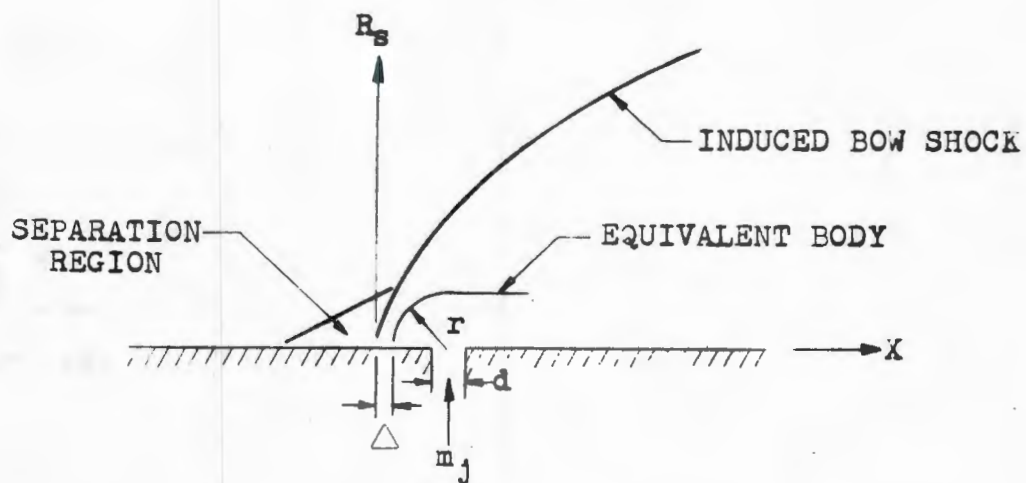


Figure 10. Hsia Flow Model.

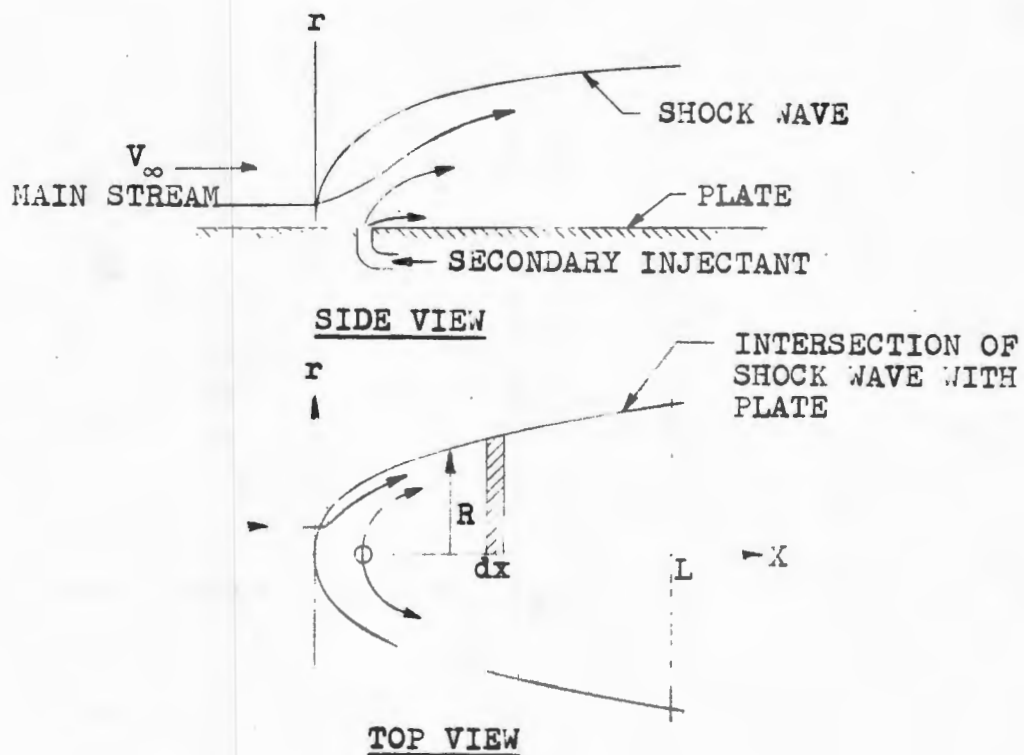


Figure 11. Broadwell Flow Model.

NITROGEN

$$\frac{P_{o,j}}{P_{o,\infty}}$$

$$d\sqrt{r} = .1376 \text{ IN.}$$

$T_{o,j}$	1	2	3	4	5	6	$3/4$	$1/2$	$1/4$
520°	1	2	3	4	5	56	10	11	12
1000°	6	7	8	9	19	57			
1500°	55	54	53	52	51	58			

$$\dot{m}_j = \text{CONSTANT}$$

$$\dot{m}_1 = .0065 \text{ lbs/sec}$$

$$\dot{m}_2 = .010 \text{ lbs/sec}$$

ARGON

$$d\sqrt{r} = .1376 \text{ IN.}$$

$$\frac{P_{o,j}}{P_{o,\infty}}$$

$T_{o,j}$	1	2	3	4	5	6
520°	25	24	23	22	21	20
1000°	27	26	48	47		
1500°	50	49				

NITROGEN

$T_{o,j}$	530°	795°	1060°	1325°	1590°	
	32	76	33	77	34	\dot{m}_1
	41	75	42	74	43	\dot{m}_2

HELIUM

$$d\sqrt{r} = .1376 \text{ IN.}$$

$$\frac{P_{o,j}}{P_{o,\infty}}$$

$T_{o,j}$	1	2	3	4	5	6
520°	31	30	69		29	28
1000°	66	64				
1500°	67	65				

ARGON

$T_{o,j}$	530°	795°	1060°	1325°	1590°	
	35	73	36	72	37	\dot{m}_1
	38	71	39	70	40	\dot{m}_2

$$\frac{P_{o,j}}{P_{o,\infty}}$$

$T_{o,j}$	1	3	5
520°	13	14	15
1000°	18	17	16
1500°	46	45	44

NITROGEN

$$d\sqrt{r} = .0735 \text{ IN.}$$

HELIUM

$T_{o,j}$	530°	795°	1060°	1325°	1590°	
	59	63	60	62	61	\dot{m}_1
	68					\dot{m}_2

FIGURE 12. Experimental Run Matrix.



Figure 13. Scillieren Photograph--Run Number 21.

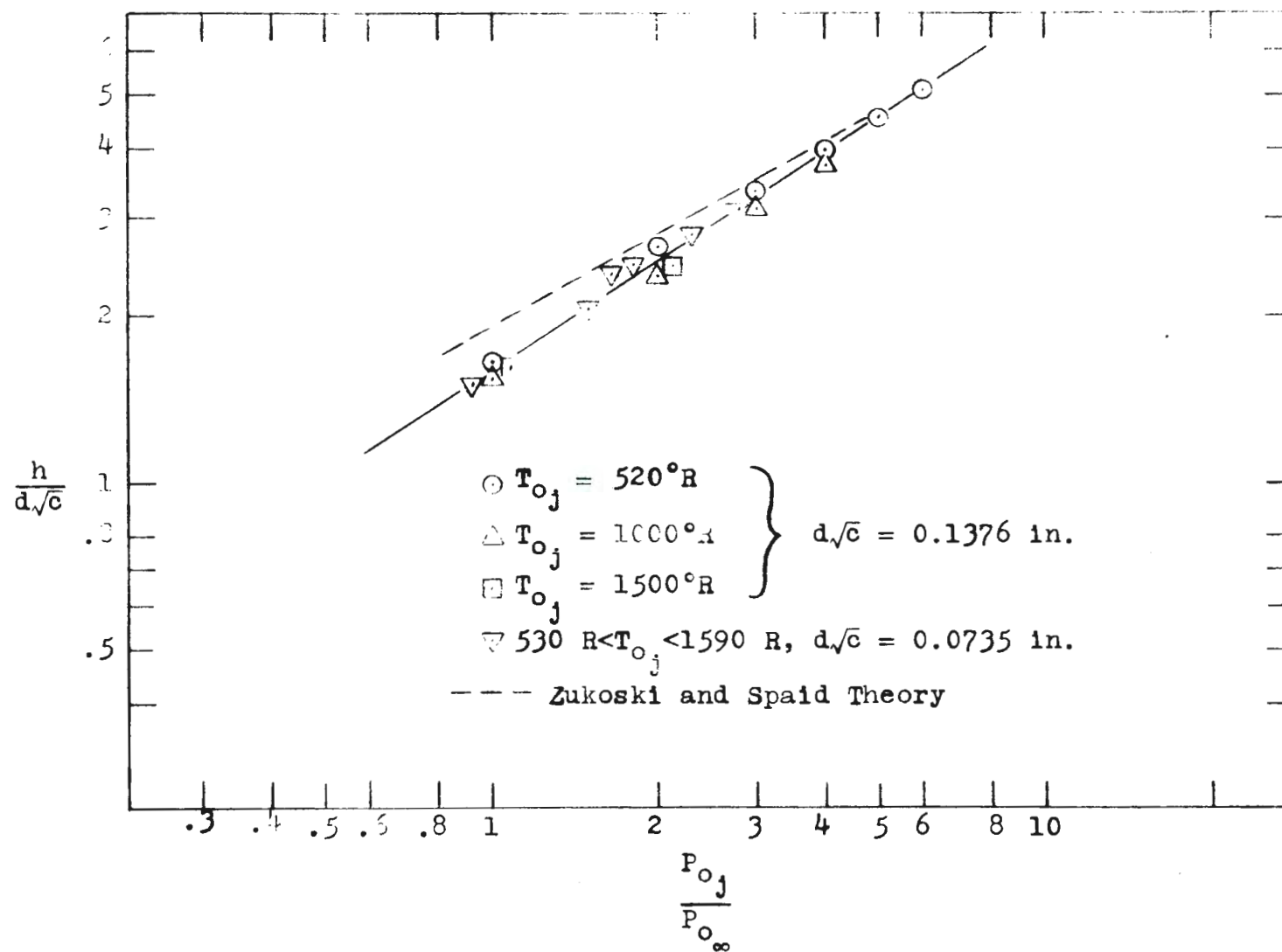


Figure 15. Penetration Height--Argon.

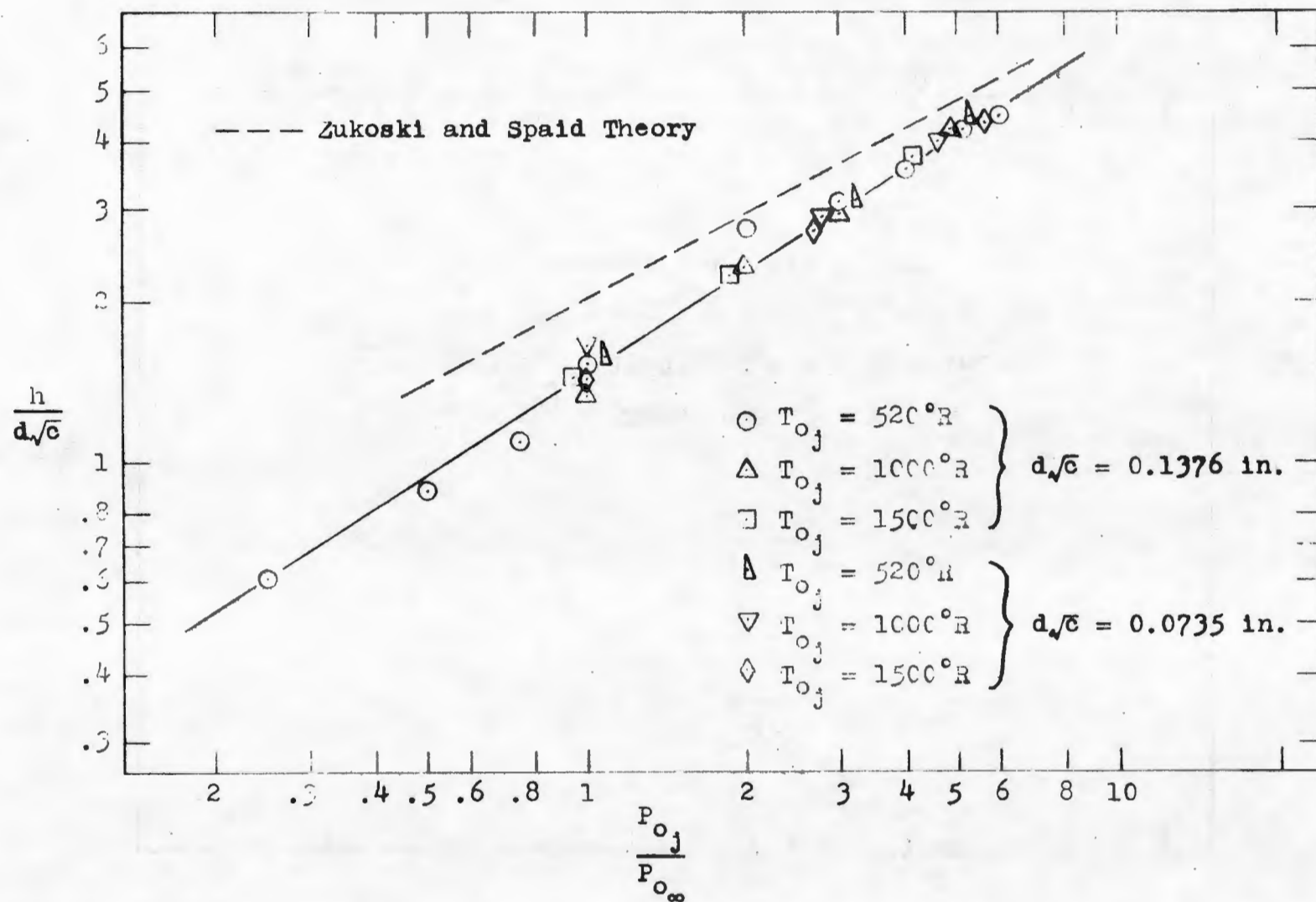


Figure 16. Penetration Height--Nitrogen.

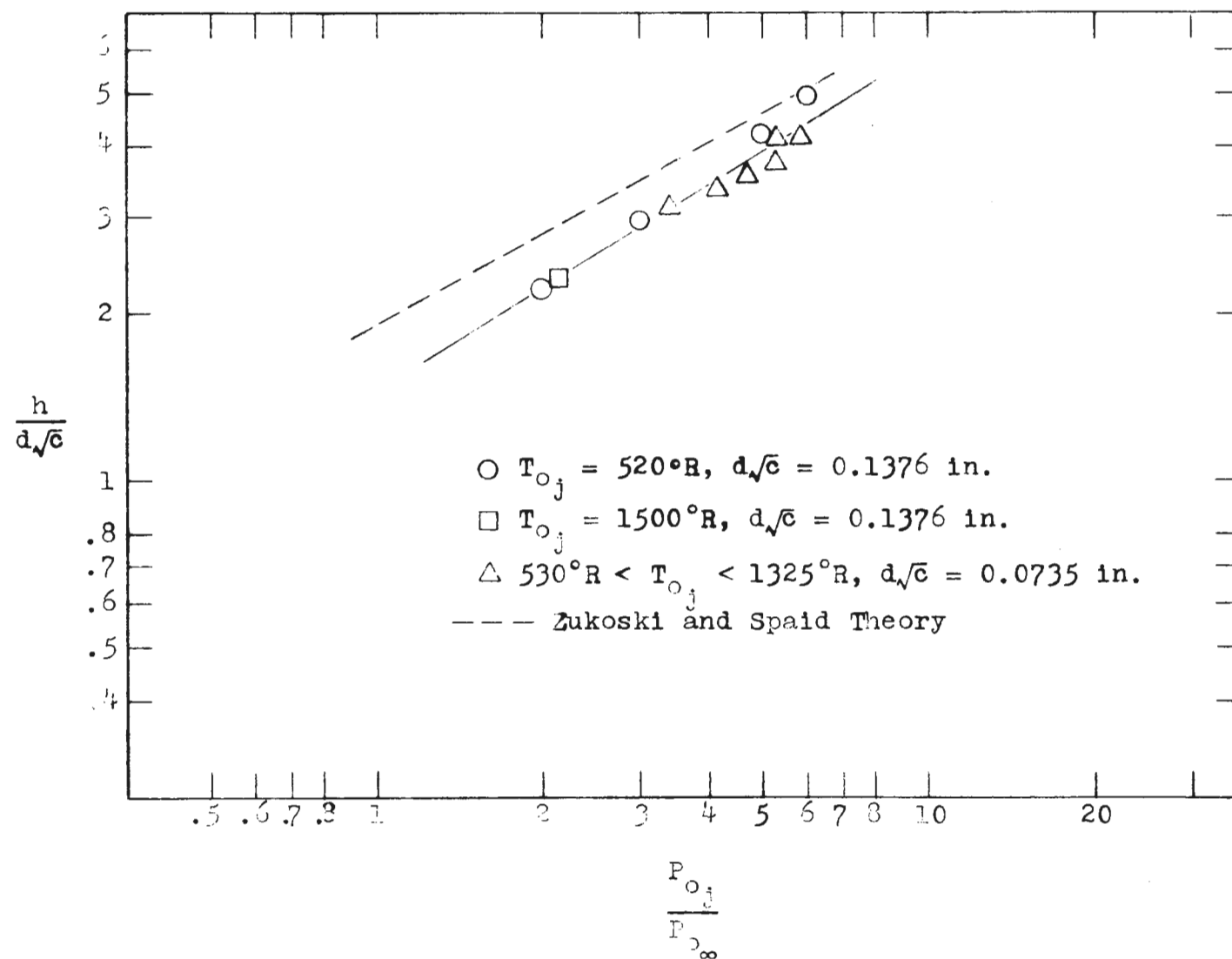


Figure 17. Penetration Height--Helium.

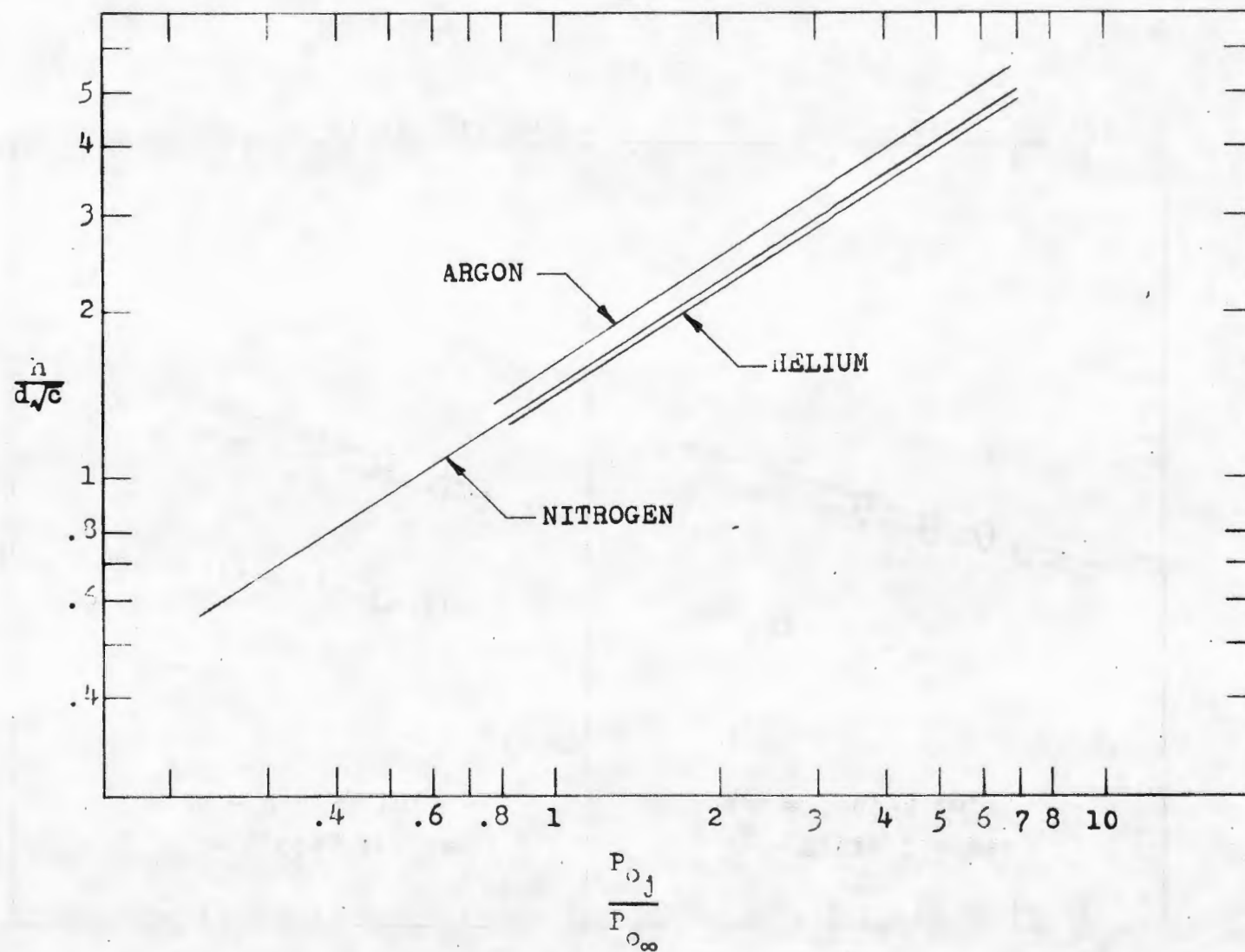


Figure 18. Composite plot of figures 15, 16 and 17.

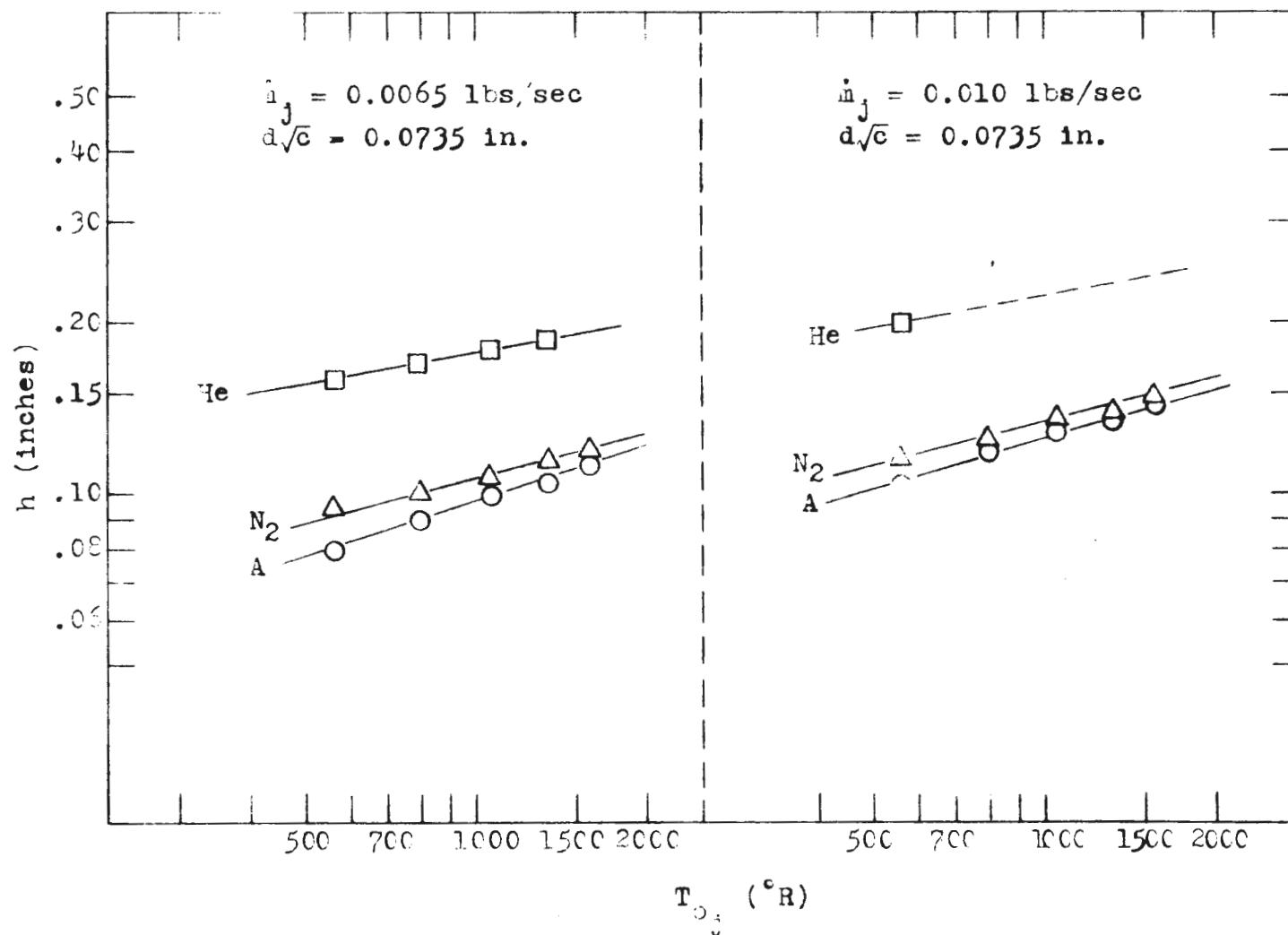


Figure 19. Penetration Height--Mass Flow Rate Constant.

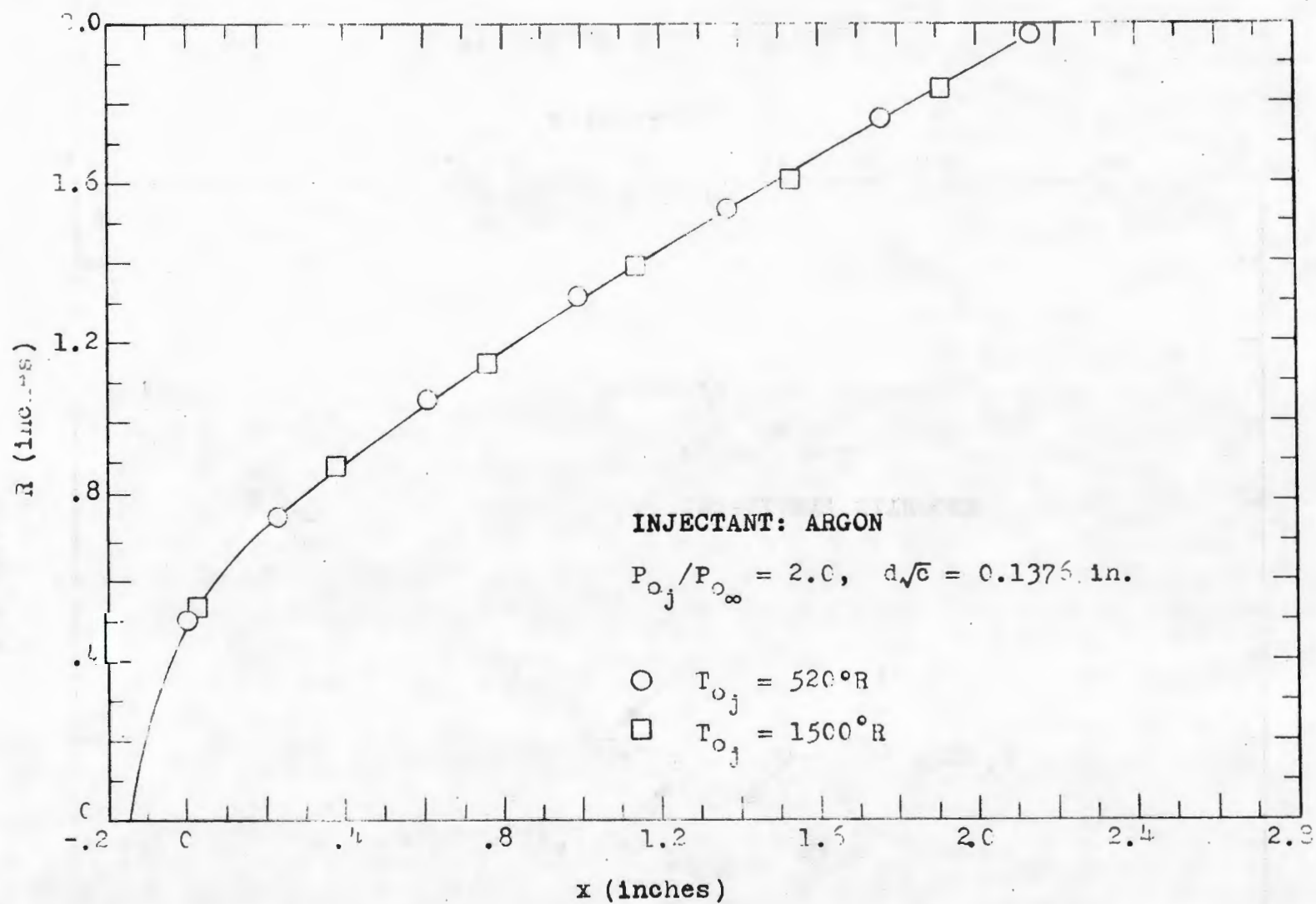


Figure 20. Shock Radius--Argon.

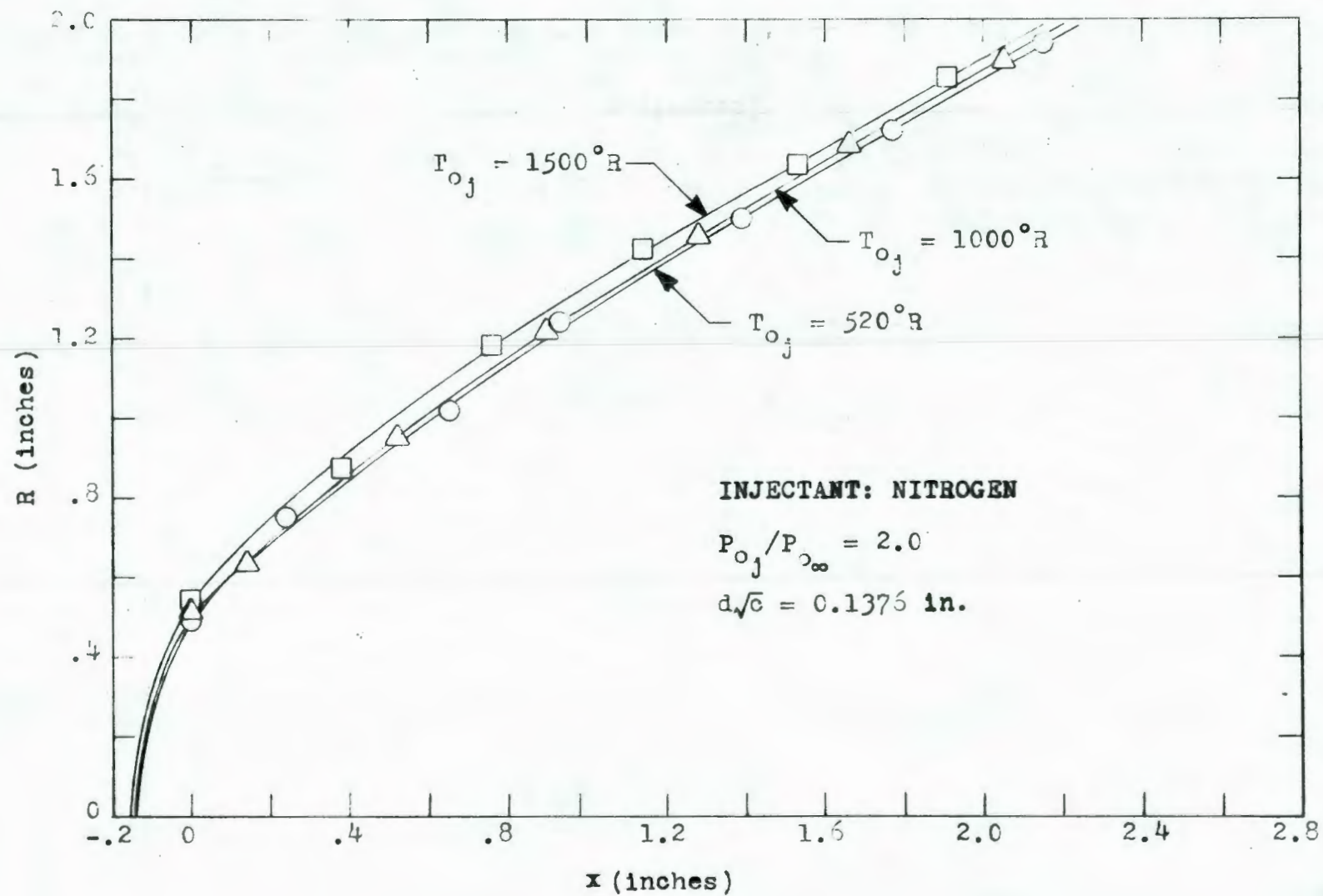


Figure 21. Shock Radius--Nitrogen.

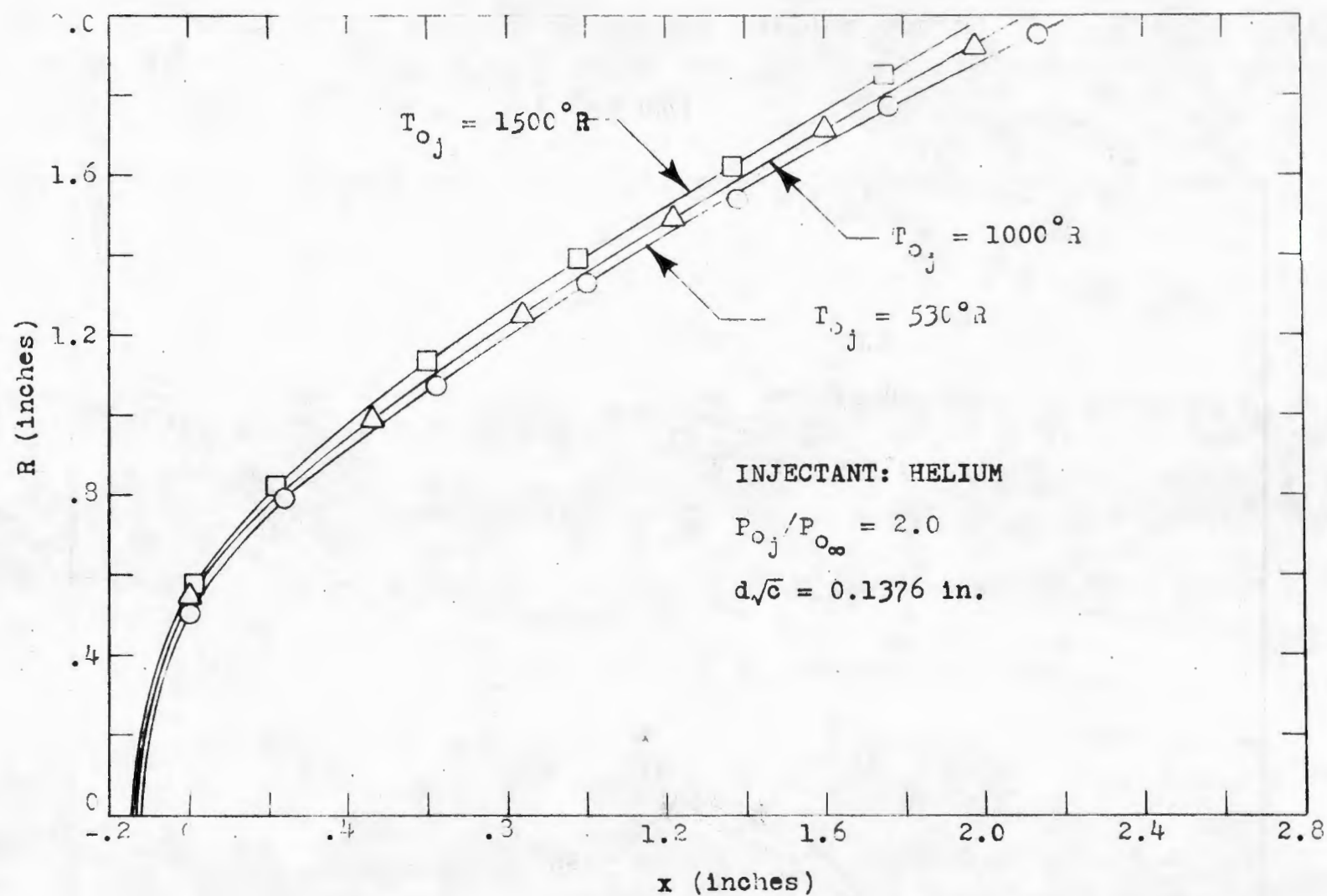


Figure 22. Shock Radius--Helium.

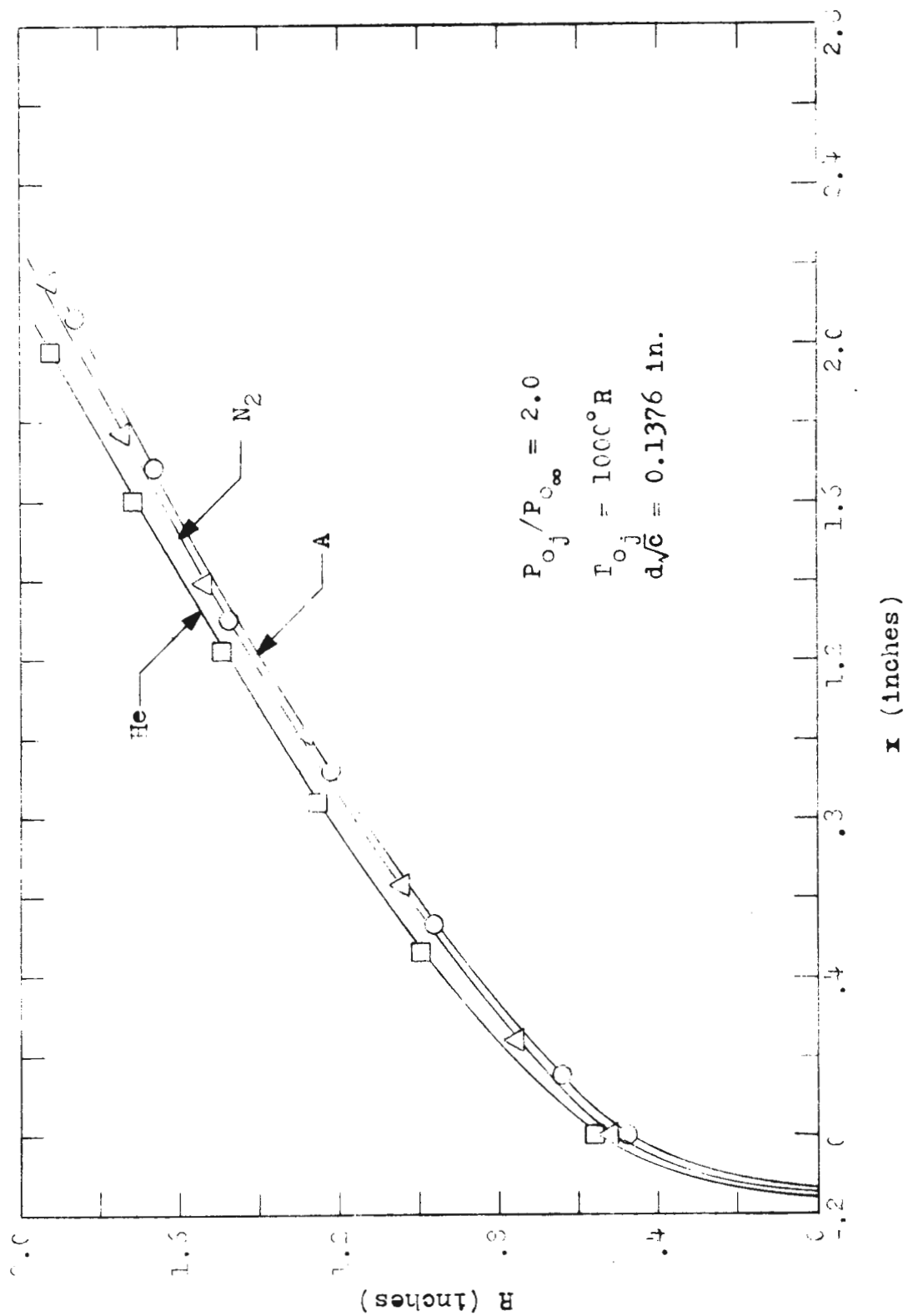


Figure 23. Shock Radius--Varying Molecular Weight.

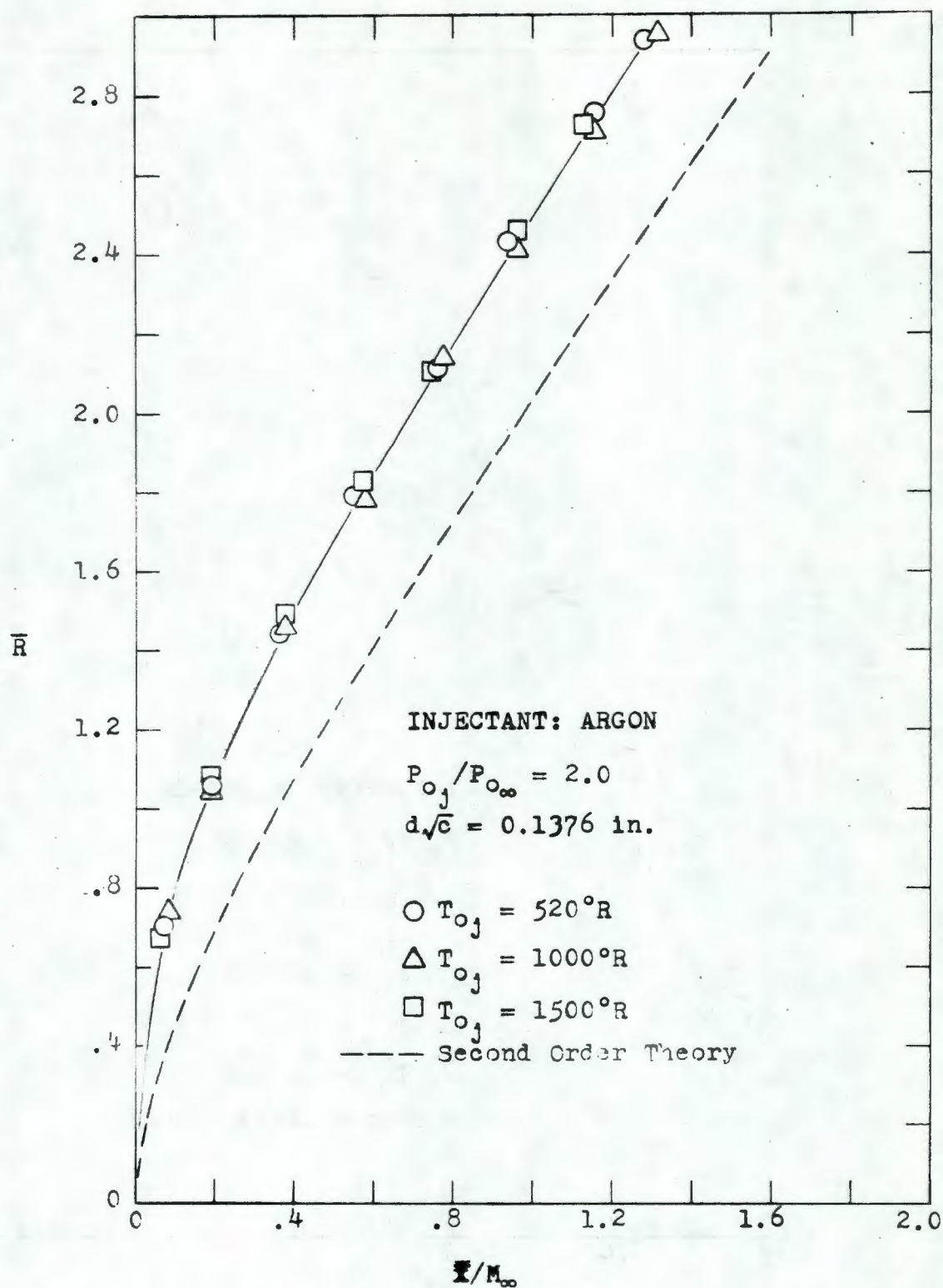


Figure 24. Non-dimensional plot of Figure 20.

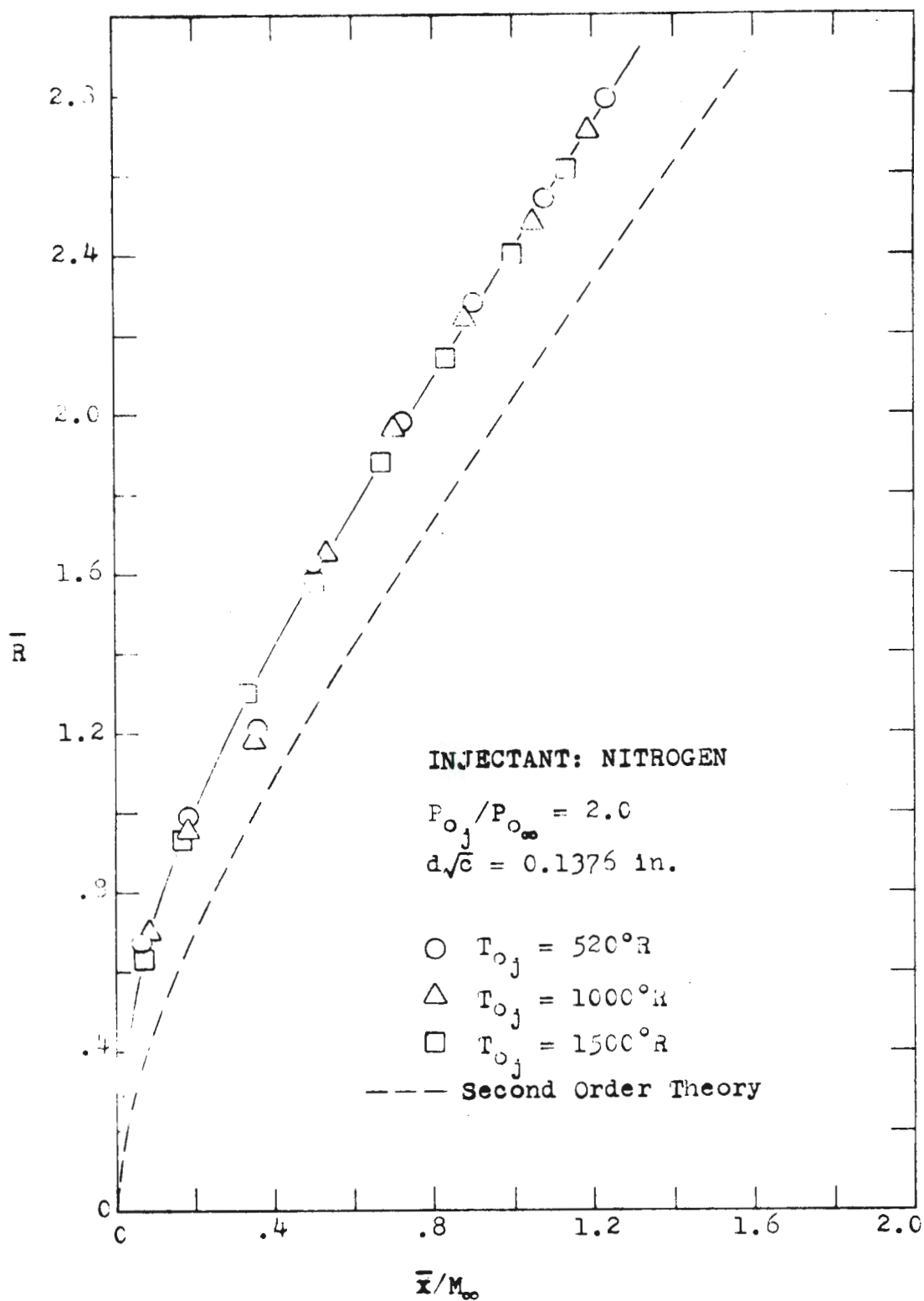


Figure 25. Non-dimensional plot of Figure 21.

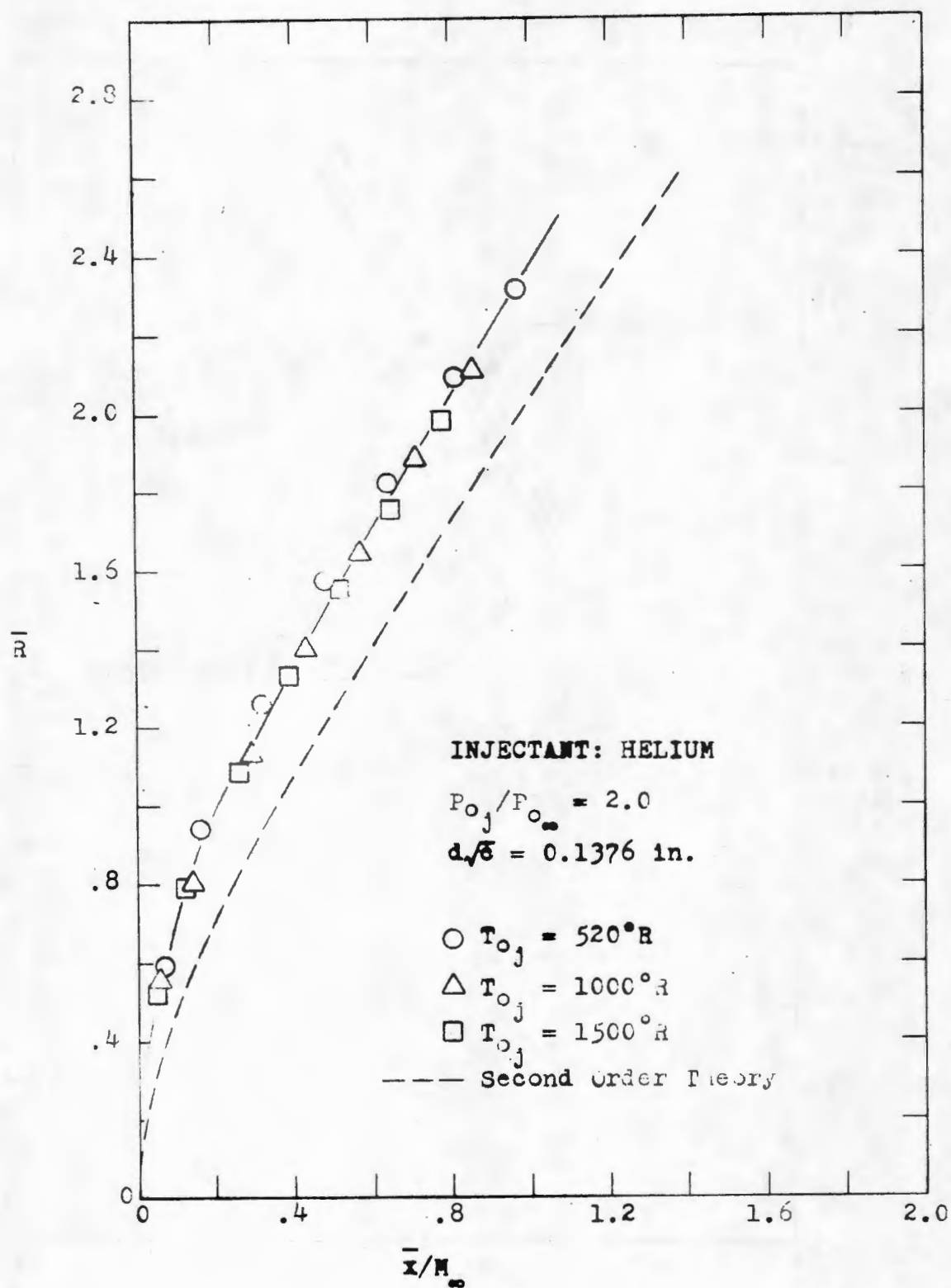


Figure 26. Non-dimensional Plot of Figure 22.

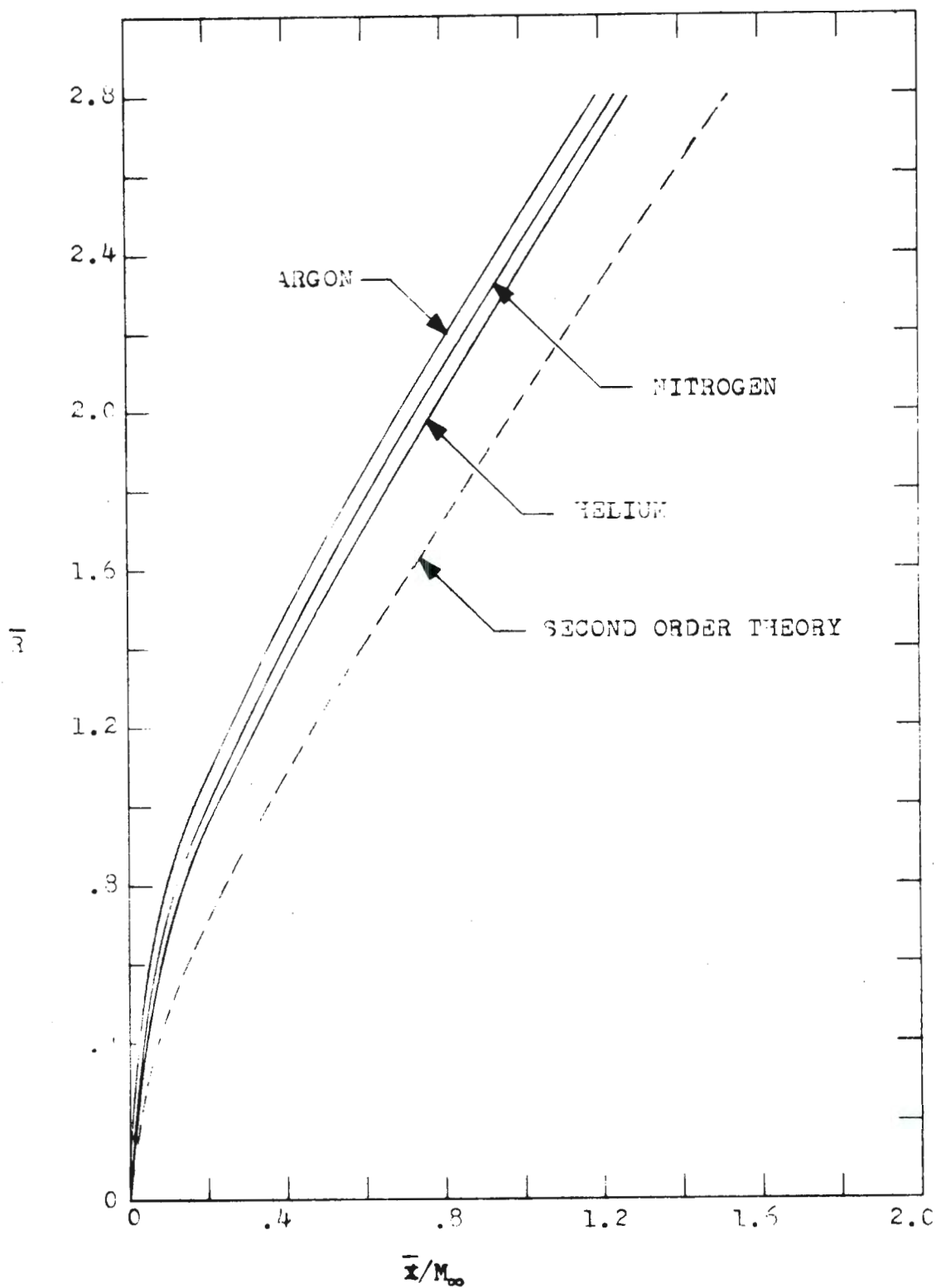


Figure 27. Composite plot of Figures 24, 25 and 26.

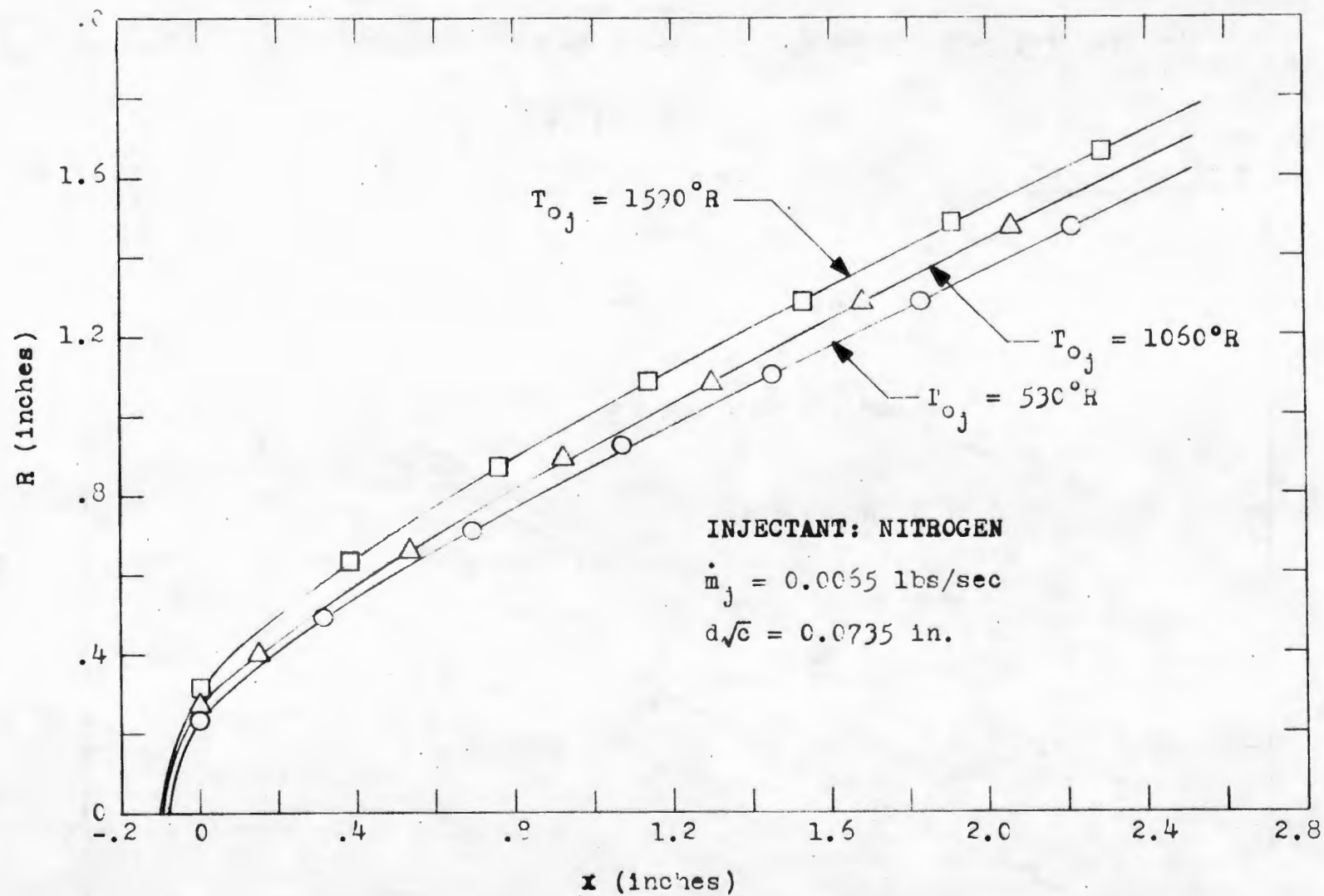


Figure 28. Shock Radius--Mass Flow Constant, Varying Temperature.

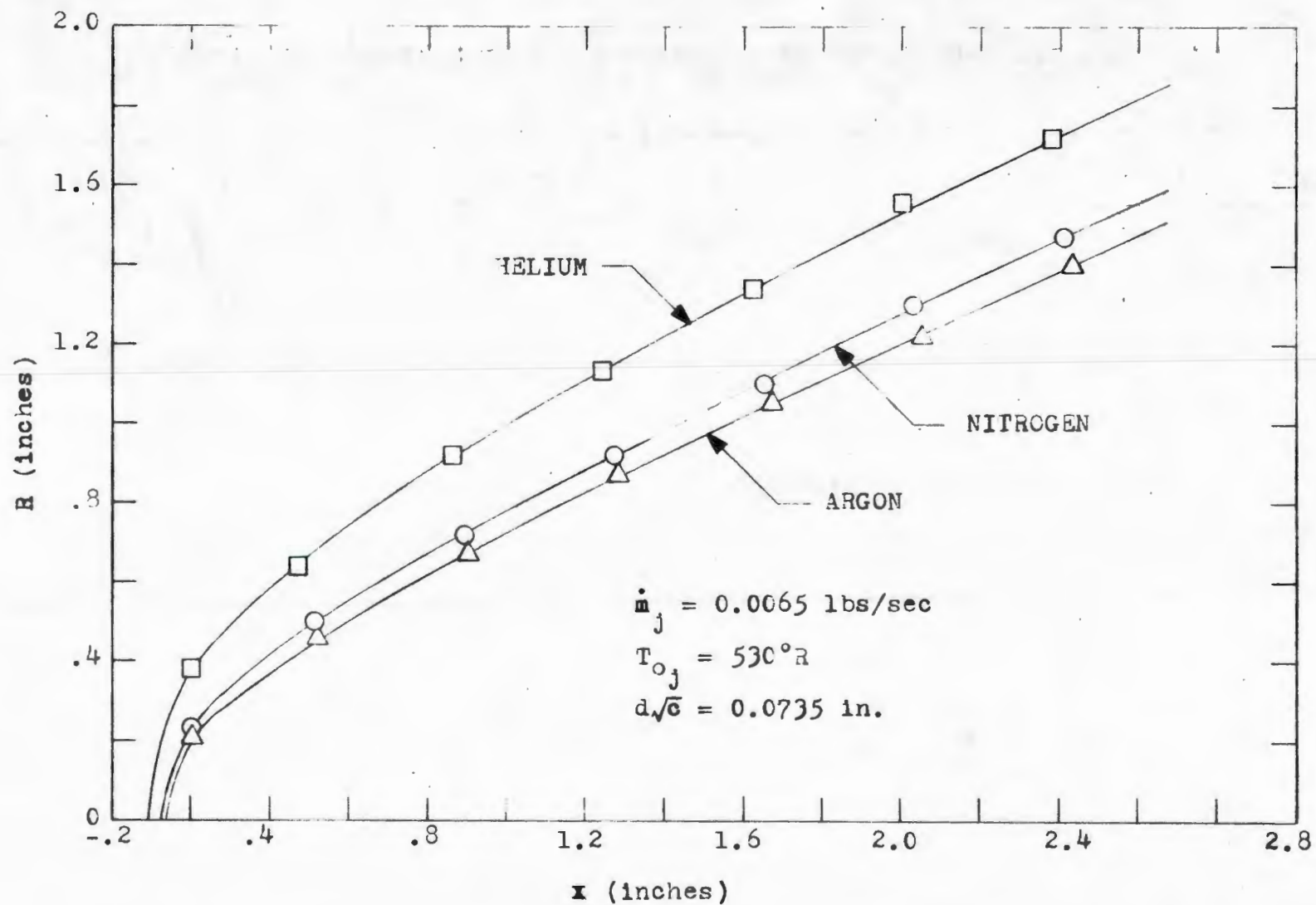


Figure 29. Shock Radius--Mass Flow Constant, Varying Molecular Weight.

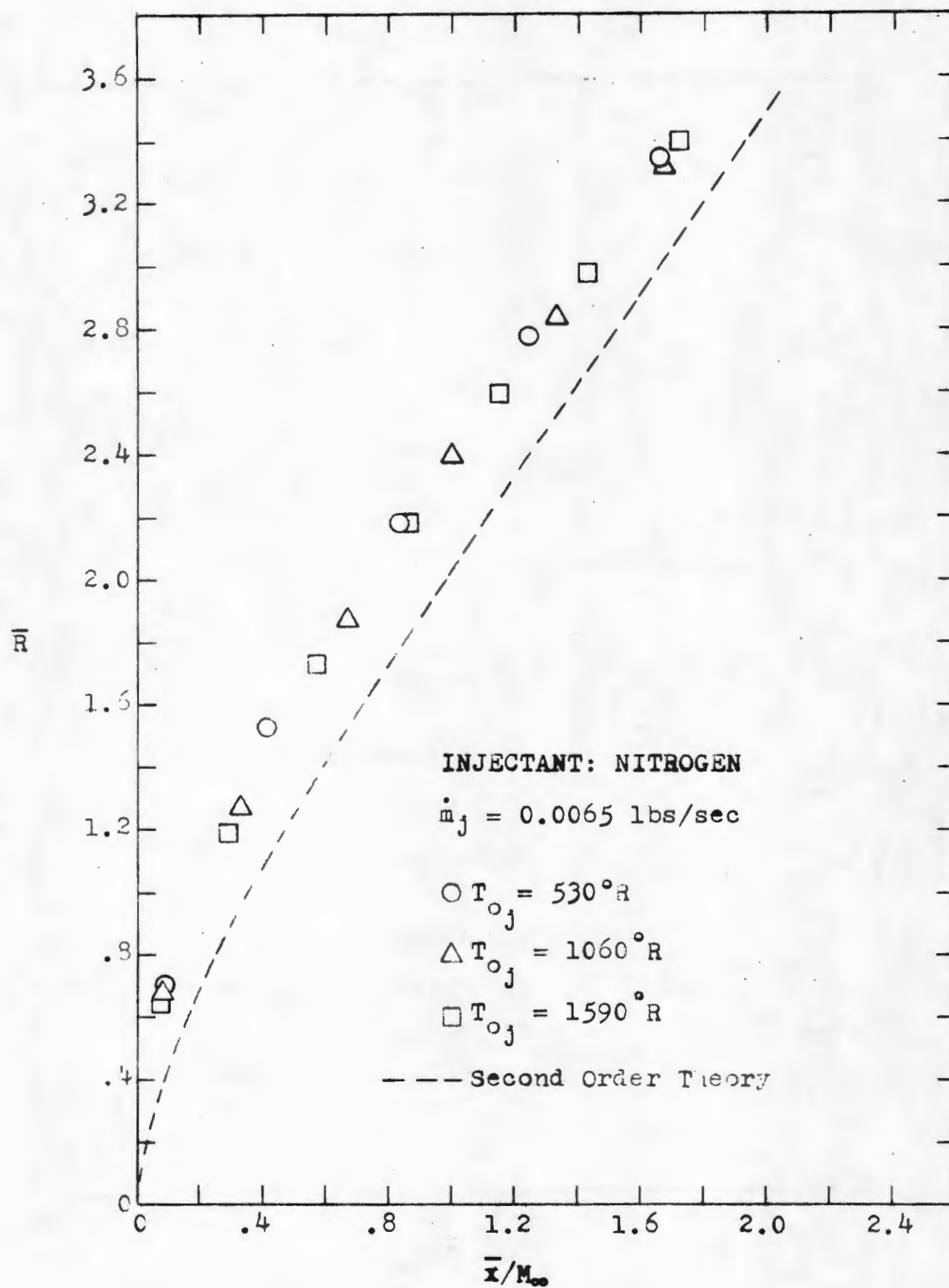


Figure 30. Non-dimensional Plot of Figure 28.

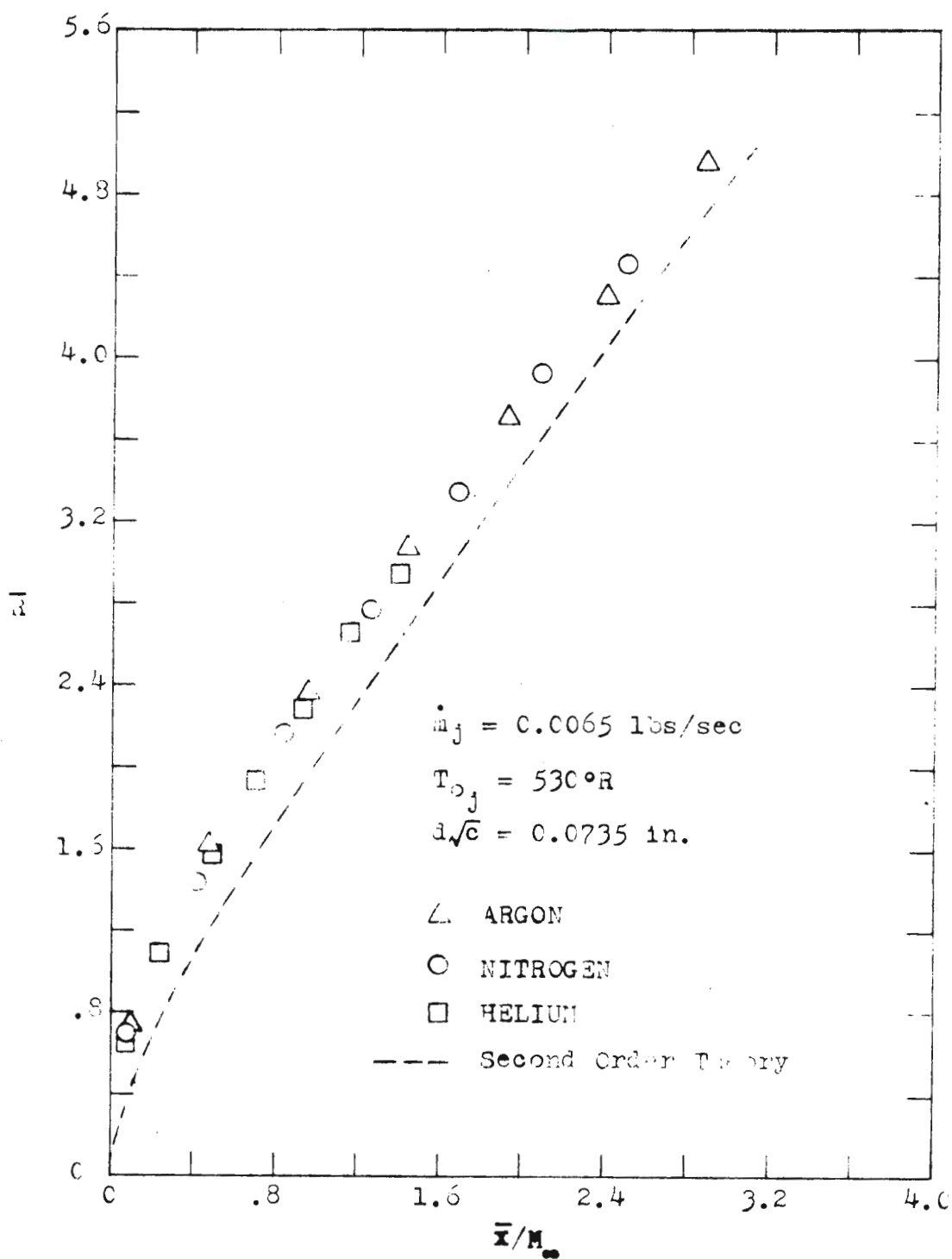


Figure 31. Non-dimensional Plot of Figure 29.

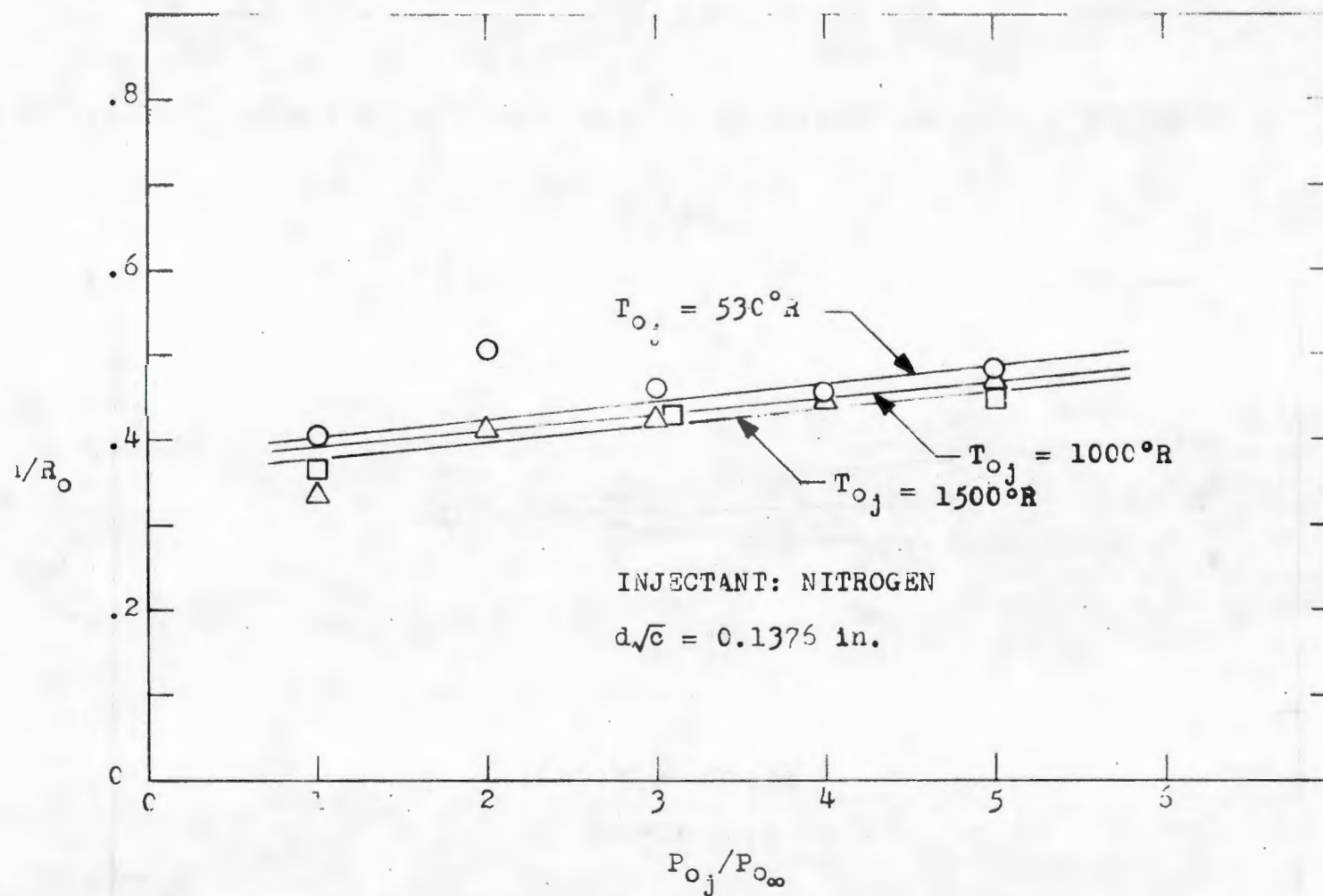


Figure 32. Comparison of Characteristic Dimensions--Varying Temperature.

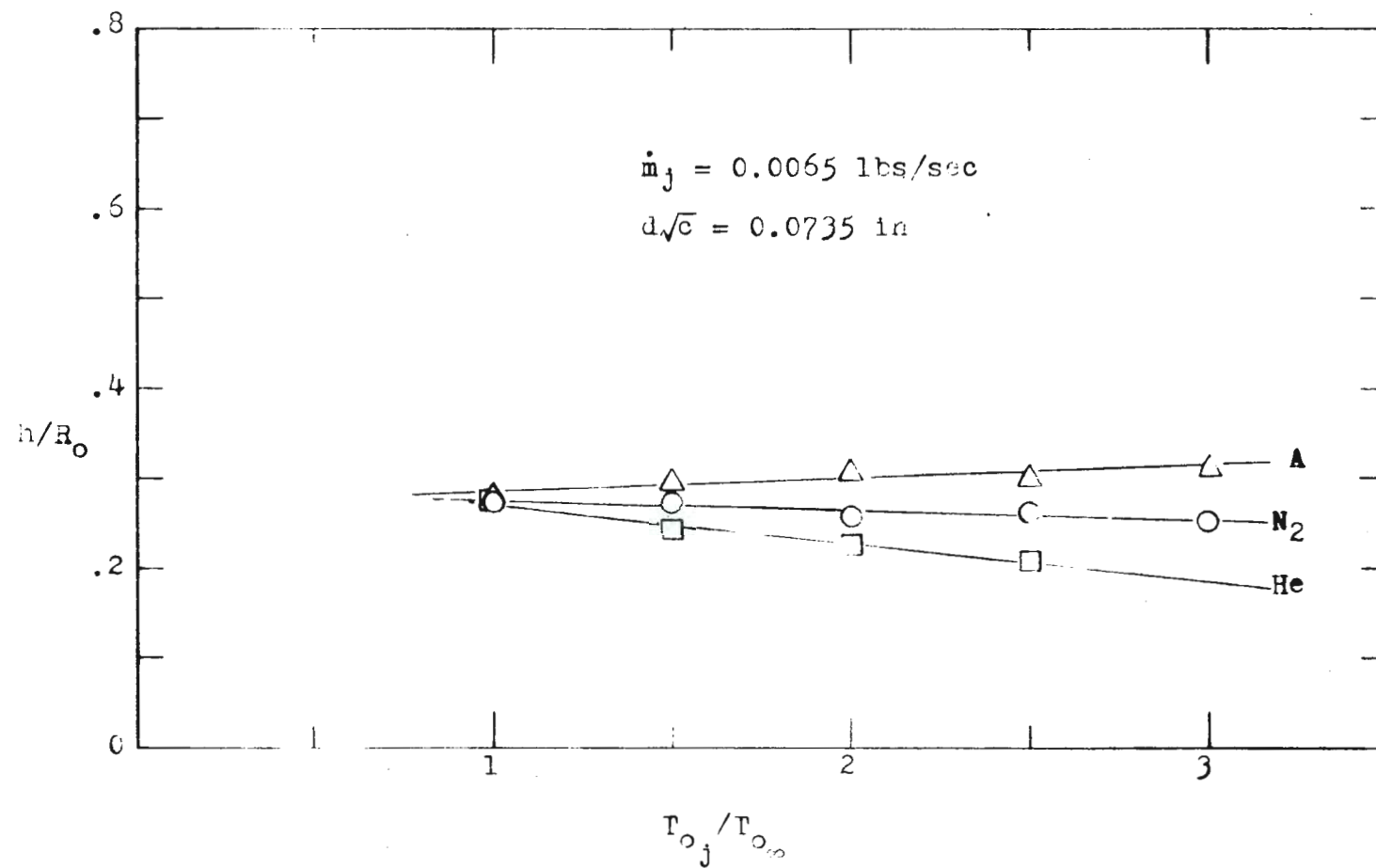


Figure 33. Comparison of Characteristic Dimensions--Mass Flow Constant.

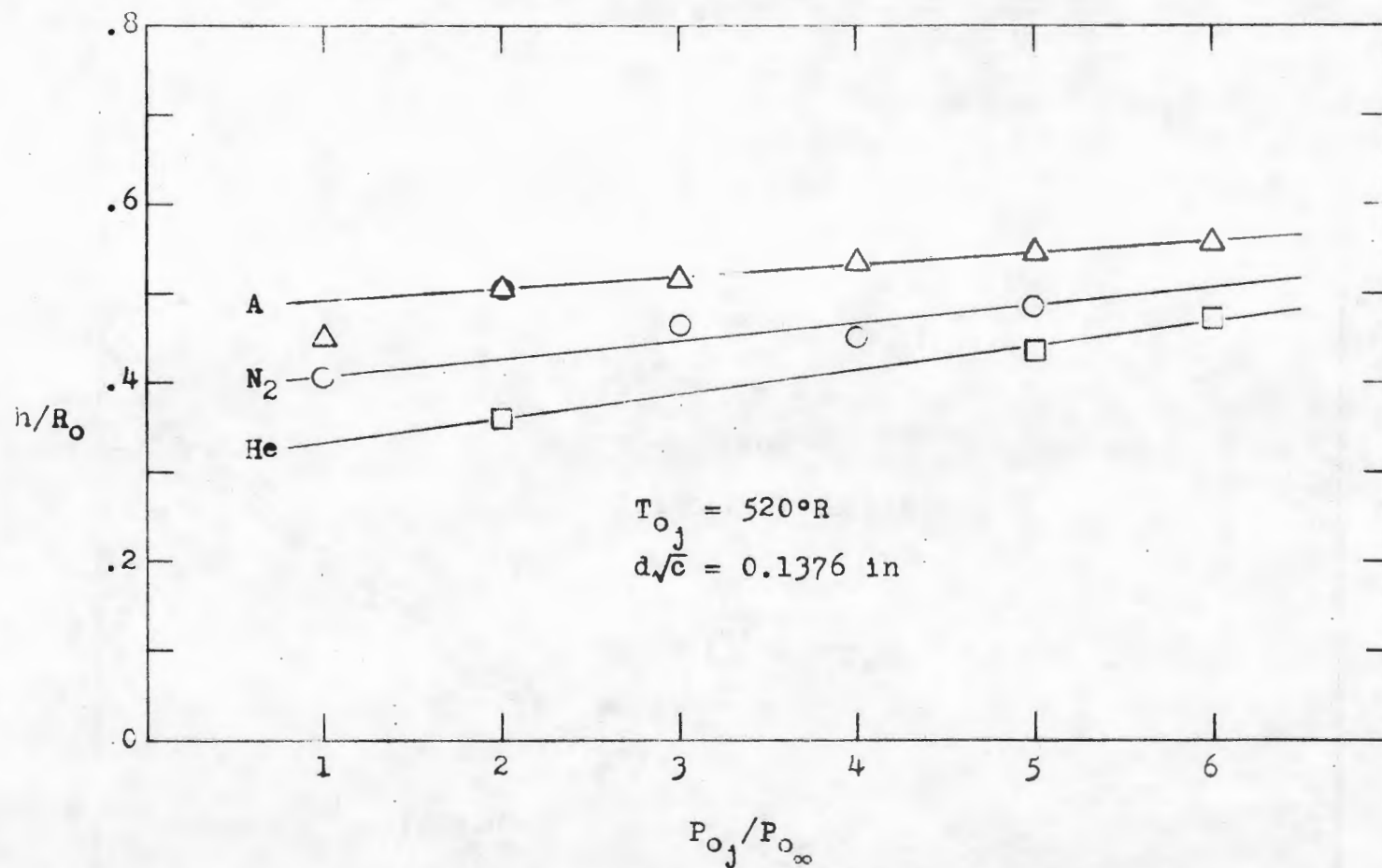


Figure 34. Comparison of Characteristic Dimensions--Varying Molecular Weight.

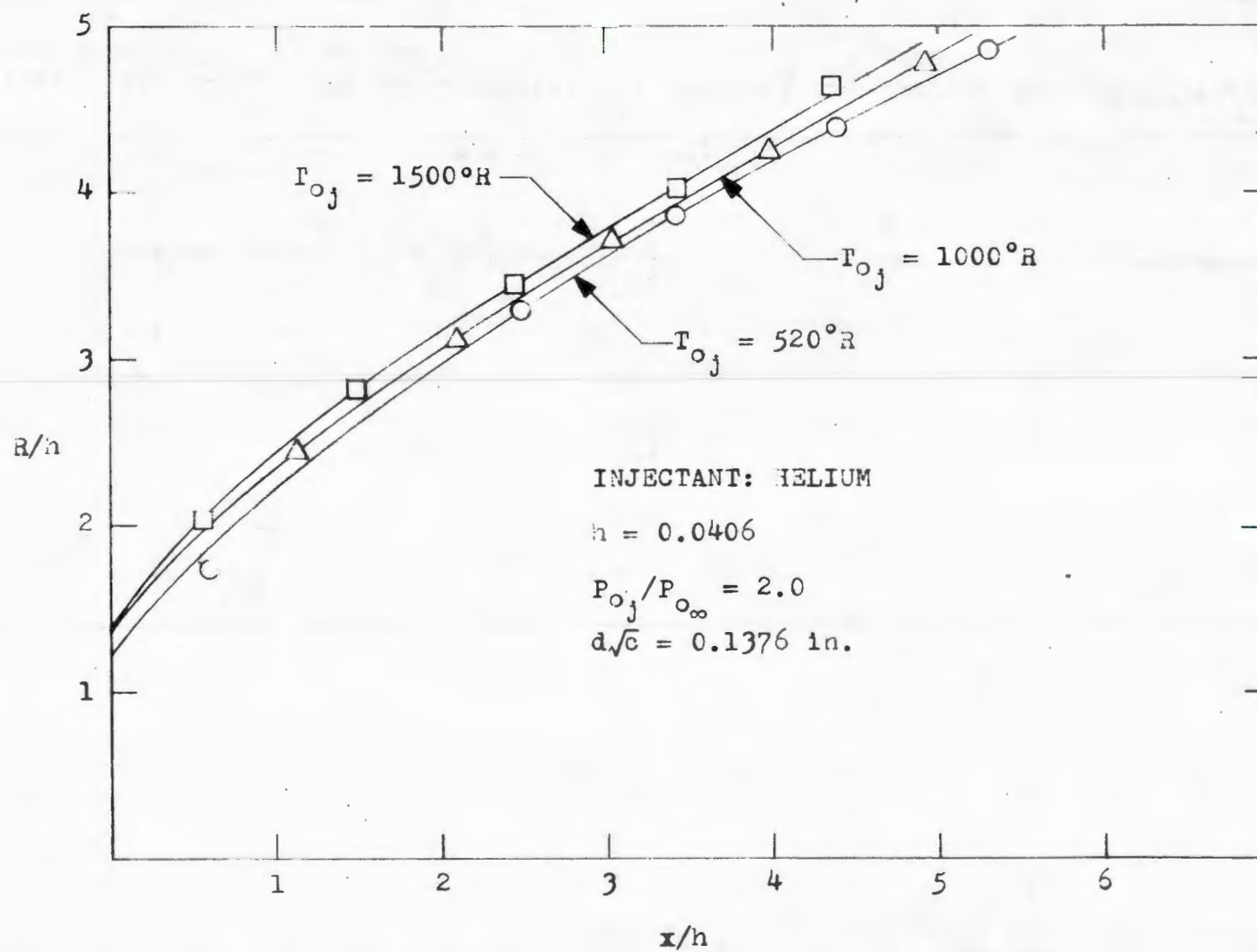


Figure 35. Shock Radius--Comparison with Penetration Height at Varying Temperature.

INITIAL DISTRIBUTION LIST

	No. Copies
1. Defense Documentation Center Cameron Station Alexandria, Virginia 22314	20
2. Library Naval Postgraduate School Monterey, California 93940	2
3. Commander, Naval Air Systems Command Navy Department Washington, D.C. 20360	1
4. Professor D. J. Collins Department of Aeronautics Naval Postgraduate School Monterey, California 93940	10
5. Chairman, Department of Aeronautics Naval Postgraduate School Monterey, California 93940	1
6. Professor A. E. Fuhs Department of Aeronautics Naval Postgraduate School Monterey, California 93940	1
7. Dr. E. S. Lamar (Code 03C) Chief Scientist, Research and Technology Naval Air Systems Command Washington, D.C. 20390	1
8. Dr. R. S. Burington Chief Mathematician Naval Air Systems Command Washington, D.C. 20390	1
9. Commander Naval Ordnance Systems Command Navy Department Washington, D.C. 20360	1
10. Office of Naval Research Navy Department Washington, D.C. 20360	1
11. Naval Air Systems Command Research and Technology Washington, D. C. 20390 Attn: Warfare Branch (Code 3031)	1

	No. Copies
12. Lt. David Wooten Department of Aeronautics Naval Postgraduate School Monterey, California 93940	2
13. Dr. Roy E. Reichenbach Room 1050, Bldg. 01 TRW Systems One Space Park Redondo Beach, California 90278	2
14. Dr. E. E. Zukoski California Institute of Technology 1201 East California Boulevard Pasadena, California 91109	1
15. Mr. Norman Leckenby Department of Aeronautics Naval Postgraduate School Monterey, California 93940	1
16. Mr. G. L. Desmond (Code 320) Aerodynamics and Structures Administration Research and Technology, Naval Air Systems Command Washington, D.C. 20390	1
17. Dr. F. I. Tanczos Technical Director, Research and Technology Naval Air Systems Command Washington, D. C. 20390	1
18. Head, Department of Engineering U.S. Naval Academy Annapolis, Maryland 21402	1
19. Superintendent U.S. Naval Academy Annapolis, Maryland 21402	1
20. Mr. I. Silver (Code 330) Propulsion Administrator Research and Technology Naval Air Systems Command Washington, D. C. 20390	1
21. Mr. R. E. Davison (Code 340) Equipment and Support Administrator Research and Technology Naval Air Systems Command Washington, D. C. 20390	1

	No. Copies
22. Mr. E. M. Fisher (Code 350) Ordnance Administrator Research and Technology Naval Air Systems Command Washington, D. C. 20390	1
23. Mr. K. G. Orman (Code 360) Command Control and Guidance Administrator Research and Technology Naval Air Systems Command Washington, D. C. 20390	1
24. Mr. I. H. Gatzke (Code 370) Surveillance Administrator Naval Air Systems Command Washington, D. C. 20390	1
25. Office of Naval Research (Code 420) Physical Sciences Division Navy Department Washington, D. C. 20360	1
26. Office of Naval Research Material Sciences Division Navy Department Washington, D. C. 20360 Attn: R. D. Cooper (Code 438)	1
27. Office of Naval Research (Code 430) Mathematical Sciences Division Navy Department Washington, D. C. 20360	1
28. Office of Naval Research Air Programs Office Navy Department Washington, D. C. 20360	1
29. Mr. E. D. Cooper (Code 303A) Advanced Systems Concepts Division Research and Technology Naval Air Systems Command Washington, D. C. 20390	1
30. Naval Air Systems Command Navy Department Washington, D. C. 20390 Attn: J. W. Malloy, Weapons Branch (Code 3033)	1

	No. Copies
31. Commander Naval Air Systems Command Headquarters Washington, D. C. 20360 AIR-03C (1) AIR-310 (1) AIR-320 (1) AIR-330B (1) AIR-536 (1) AIR-5366 (1) AIR-5367 (1) AIR-538 (1)	8
32. Commander Naval Ordnance Systems Command Headquarters Washington, D. C. 20360 ORD-03B (1) ORD-033 (1)	2
33. Chief of Naval Research Dr. Ralph Roberts (Code 429) Navy Department Washington, D. C. 20360	1
34. Naval Ordnance Station Dr. G. Testi (Code RR) Indian Head, Maryland 20640	
35. Army Missile Command Research and Development Directorate Redstone Arsenal Huntsville, Alabama 35809 Propulsion Laboratory, F. James (1) Library (1)	2
36. Commander Naval Weapons Center China Lake, California 93555 Code 608 (1) Code 451 (1) Code 458 (1) Library (1)	4

	No. Copies
37. Commander Naval Ordnance Laboratory White Oak Silver Spring, Maryland 20910 Code 310 (1) Library (1)	2
38. Commanding Officer and Director Naval Ships Research and Development Center Washington, D. C. 20007 Code 600 (1) Library (1)	2
39. Applied Physics Laboratory 8621 Georgia Avenue Silver Spring, Maryland 20910 Library (1) Aeronautics Division (2) CPIA (1)	4
40. LTCOL F. B. Alford, SCTTI Air Force Systems Command Andrews Air Force Base Washington, D. C. 20331	1
41. Air Force Aero-Propulsion Laboratory Wright-Patterson Air Force Base, Ohio 45433 APG (1) APX (1)	2
42. Air Force Armament Laboratory Eglin Air Force Base, Florida 32544 ATW (1) ATZ (1)	2
43. Air Force Rocket Propulsion Laboratory Edwards AFB, California 93523 RPM (1) RPMC (1) RPPP (1) RPR (1) RPRE (1) RPRP (1) RPX (1)	7

	No. Copies
44. Air Force Flight Dynamics Laboratory Wright-Patterson Air Force Base, Ohio 45433	1
45. CO, Navy Space Systems Activity Hq. Air Force Space Systems Division Air Force Unit Post Office Los Angeles, California 90045	1
46. Lt. Larry J. Chrans, USN VA-122, NAS Lemoore Lemoore, California 92135	3

Security Classification

14

KEY WORDS

LINK A

LINK B

LINK C

ROLE

WT

	ROLE
Chairman	Mr. J. Edgar Hoover
Vice Chairman	Mr. Clegg
Members	Mr. Glavin Mr. Ladd Mr. Nichols Mr. Rosen Mr. Tracy Mr. Carson Mr. Egan Mr. Gurnea Mr. Hendon Mr. Pennington Mr. Quinn Tamm Mr. Nease Mr. Mohr Mr. Winterrowd Miss Gandy

WT

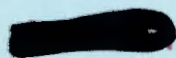
NAME	ROLE
Mr. J. Edgar Hoover	Director
Mr. Clegg	Chief of Bureau
Mr. Glavin	Chief of Bureau
Mr. Ladd	Chief of Bureau
Mr. Nichols	Chief of Bureau
Mr. Rosen	Chief of Bureau
Mr. Tracy	Chief of Bureau
Mr. Carson	Chief of Bureau
Mr. Egan	Chief of Bureau
Mr. Gurnea	Chief of Bureau
Mr. Hendon	Chief of Bureau
Mr. Pennington	Chief of Bureau
Mr. Quinn	Chief of Bureau
Mr. Nease	Chief of Bureau
Mr. Gandy	Chief of Bureau

WT

Supersonic Injection

DD FORM 1473 (BACK)
1 NOV 65
S/N 0101-807-6821

UNCLASSIFIED
Security Classification



thesC4489

The effect of stagnation temperature and

DUDLEY KNOX LIBRARY



3 2768 00421995 6

DUDLEY KNOX LIBRARY